

Polymerized spacetime dynamics with multi-field source: unraveling the pre-inflationary Universe

Divya Gupta,^{1,*} Manabendra Sharma,^{1,†} Gustavo S. Vicente,^{2,‡} Rudnei O. Ramos,^{3,§} and Anzhong Wang^{4,¶}

¹*Centre for Theoretical Physics and Natural Philosophy,*

Nakhonsawan Studiorum for Advanced Studies, Mahidol University, Nakhonsawan 60130, Thailand

²*Faculdade de Tecnologia, Universidade do Estado do Rio de Janeiro, 27537-000 Resende, RJ, Brazil*

³*Departamento de Física Teórica, Universidade do Estado do Rio de Janeiro, 20550-013 Rio de Janeiro, RJ, Brazil*

⁴*GCAP-CASPER, Department of Physics & Astronomy, Baylor University, Waco, Texas 76798-7316, USA*

We study a multi-field model in Loop Quantum Cosmology for a maximally symmetric spacetime governed by the Einstein–Hilbert action minimally coupled to scalar fields. Using a Legendre transformation, we formulate the Hamiltonian dynamics in canonically equivalent geometrodynamical and Yang–Mills–type representations, incorporating nontrivial couplings through a geometric structure on the multi-field configuration space. Implementing the $\bar{\mu}$ -scheme polymerization, we obtain the loop-quantum-corrected Friedmann equations. By focusing on the two-field model as an example, we analyze the effective dynamics for specific potentials. The *quantum bouncing, transition, and slow-roll inflationary* phases are investigated numerically, and viability of the models is assessed by evaluating the number of e-folds during the inflationary phase for certain given initial conditions. The global behavior of the background evolution is further examined through linear stability and dynamical-systems analyses.

CONTENTS

I. Introduction	1
II. Dynamics for multi-field Scenario	2
A. Classical formulation	2
B. Quantum Corrected Dynamics via Polymerization	4
C. Background dynamics	4
III. Models	5
A. Hybrid inflation	5
B. String-inspired model	6
IV. Background dynamics for the hybrid inflation	7
A. Numerical analysis	7
B. Qualitative Analysis: Dynamical System Approach	13
V. Background dynamics for the string-inspired model	18
A. Numerical analysis	18
B. Qualitative Analysis: Dynamical System Approach	28
VI. Conclusion	29
Acknowledgments	30

A. Analytical solutions to the background dynamics	30
References	32

I. INTRODUCTION

Loop Quantum Cosmology (LQC), obtained by applying LQG techniques to symmetry-reduced spacetimes, provides an effective framework for investigating high-curvature regimes of the early universe [1–3]. A key prediction of LQC is the resolution of the classical big bang singularity, which is replaced by a non-singular quantum bounce [4–14]. This phenomenon arises purely from quantum geometric effects, without invoking exotic matter or modifications to general relativity (GR). In this scenario, classical divergences in energy density and curvature are naturally regulated by the existence of a minimal, nonzero eigenvalue for the area operator—a consequence of the underlying discrete geometry. The robustness of singularity resolution in LQC extends beyond Einstein–Hilbert gravity and has been established for non-trivial spacetimes, different cosmologies including the ones exhibiting anisotropic cosmologies [15–26].

Interestingly, such an effective setup naturally leads to a phase of slow-roll inflation following the quantum bounce [27–32]. Over the past two decades, a substantial body of work has explored this single-field framework in LQC, covering a variety of inflationary potentials and analyzing their implications for early-universe dynamics, see, for example, [16, 33–37] and references therein, but only a limited number of works have considered multi-field systems [38]. However, to the best of our knowledge, multi-field scenarios, particularly with non-trivial

* divya920818@gmail.com

† Corresponding author; sharma.man@mahidol.ac.th

‡ gustavo@fat.uerj.br

§ rudnei@uerj.br

¶ Anzhong_Wang@baylor.edu

field-space geometry have not been extensively investigated within the effective dynamics of LQC. In this work, we aim to address this gap by studying the coupled dynamics of multiple scalar fields in a holonomy corrected cosmological background.

Scalar field theory has long served as a foundational tool for constructing cosmological models, especially those aimed at realizing inflationary dynamics. Moreover, the dynamical richness increases when the non-trivial metric of multi-field space and cross-coupling terms between scalar fields are introduced [39–43].

Traditional slow-roll models can face fine-tuning issues [44], while purely kinematic models like hyperinflation may not terminate naturally [43]. This is where Linde’s hybrid inflation paradigm becomes relevant [45]. By coupling the inflaton to a "waterfall" field, inflation ends abruptly via a symmetry-breaking instability when the inflaton crosses a critical value, a mechanism controlled by potential dynamics rather than the gradual failure of slow-roll [45]. Subsequent studies have shown that the successful trajectories in hybrid models form a fractal attractor in field space, making inflation generic for a broad range of initial conditions [46]. Moreover, hybrid inflation has been successfully embedded within supersymmetric and supergravity frameworks, improving their alignment with particle physics and observational constraints [44, 47].

In LQC, where quantum gravitational corrections such as inverse volume and holonomy effects significantly alter the early universe’s dynamics [5, 48–52], it becomes essential to understand how these multi-field inflationary mechanisms behave. Since LQC modifies Friedmann dynamics, the collective behavior of scalar fields could offer new insights into early universe acceleration, attractor behavior, and potentially distinguishable phenomenological signatures from standard inflationary cosmology.

In this paper, our main interest is to understand the background dynamics of multifield scalar models in the context of LQC. We will focus on two representative multi-field inflationary scenarios in this paper: the hybrid inflation potential and an interacting two-field potential model. We analyze the background dynamics of both models within the framework of LQC and assess their viability, i.e., for producing sufficient inflation, when initial conditions are set at the bounce instant.

This paper is organized as follows. In Sec. II we briefly review both the classical and quantum formulations appropriate for the multifield models, leading to their background dynamics in LQC. In Sec. III, we present the two representative multifield models we study in this work: a two-field model as used hybrid inflation and a model inspired in string theory, which displays kinetic interaction between the fields. The numerical analysis of the hybrid model is presented in Subsec. IV A, while in Subsec. V A the detailed analysis for the second model is presented. Finally, our conclusions and future perspectives are summarized in Sec. VI.

II. DYNAMICS FOR MULTI-FIELD SCENARIO

In this section, we first review the classical formulation of a generic minimally coupled multi-field scenario in connection to dynamics for Friedmann–Lemaître–Robertson–Walker (FLRW) spacetime. Then at the end we present its quantization leading to the LQC dynamics.

A. Classical formulation

We begin with the Einstein-Hilbert action,

$$S = \int d^4x \sqrt{-g} \left[\frac{1}{2\kappa} R - \frac{1}{2} G_{IJ}(\phi^K) \partial_\mu \phi^I \partial^\mu \phi^J - V(\phi^K) \right]. \quad (2.1)$$

where $\kappa = 8\pi/m_{\text{Pl}}^2$, with m_{Pl} is the Planck mass, g is the determinant of metric $g_{\mu\nu}$, R is the scalar curvature term obtained from the trace of the Ricci tensor $R_{\mu\nu}$, $G_{IJ}(\phi^K)$ is the metric living in the space of scalar fields [53] and $V(\phi^K)$ is the multi-field potential. This represents a special case of non-canonical scalar field scenario [54], where a non-trivial choice of G_{IJ} introduces a non-Euclidean field-space geometry and hence non-canonical kinetic term, with $G_{IJ} = \delta_{IJ}$ representing the canonical limit.

In conformity with the cosmological principle, we invoke the FLRW metric:

$$ds^2 = -N^2(t) dt^2 + a(t)^2 (dx^2 + dy^2 + dz^2), \quad (2.2)$$

to describe the homogeneous and isotropic universe, where $N(t)$ is the lapse function. Throughout this work, we consider the gauge $N(t) = 1$. The background dynamics is governed by the Einstein field equations and Klein-Gordon equations for each field ϕ^K [53],

$$3H^2 = \kappa \left(\frac{\dot{\sigma}^2}{2} + V(\phi^K) \right), \quad (2.3a)$$

$$\dot{H} = -\frac{\kappa \dot{\sigma}^2}{2}, \quad (2.3b)$$

$$D_t \dot{\phi}^K + 3H \dot{\phi}^K + G^{IK} V_{,I}(\phi^I) = 0, \quad (2.3c)$$

where overdot means derivative w.r.t. cosmic time, $H \equiv \frac{\dot{a}}{a}$ is the Hubble parameter, $\dot{\sigma}^2/2$ is the total kinetic energy, where σ is the “adiabatic field” which represents the path length along the trajectory, such that $\dot{\sigma}^2 = G_{IJ} \dot{\phi}^I \dot{\phi}^J$, $V_{,I}(\phi^I) \equiv \frac{\partial V}{\partial \phi^I}$, and D_t is the covariant derivative in the multi-field space, defined as $D_t A^I \equiv \dot{A}^I + \Gamma_{JK}^I \phi^J \dot{A}^K$, where Γ_{JK}^I are the Christoffel symbols compatible with the multi-field metric G_{IJ} [53].

¹ The field-space metric G_{IJ} is symmetric, $G_{IJ} = G_{JI}$ [53], and admits an inverse G^{IJ} satisfying $G^{IK} G_{KJ} = \delta^I_J$.

From the resultant kinetic term $\dot{\sigma}^2/2$, the total energy and pressure density, respectively, read as

$$\rho = \frac{\dot{\sigma}^2}{2} + V(\phi^K), \quad (2.4)$$

$$P = \frac{\dot{\sigma}^2}{2} - V(\phi^K). \quad (2.5)$$

From the Ricci scalar $R = 6 \left(\frac{\dot{a}}{a} + \frac{\dot{a}^2}{a^2} \right)$ and using $\sqrt{-g} = a^3$, the Lagrangian density \mathcal{L} is reduced to:

$$\mathcal{L} = -\frac{3\dot{a}^2 a}{\kappa} + \frac{a^3}{2} G_{IJ} \dot{\phi}^I \dot{\phi}^J - a^3 V(\phi^K). \quad (2.6)$$

The configuration space of the Lagrangian density consists of (a, ϕ^K) , with K corresponding to the number of fields in the multi-field space. In order to obtain the quantum corrected dynamics via LQG technique, the present theory must be canonically formulated. For this, we need to transform the configuration space to phase space, i.e., $(a, \phi^K) \rightarrow (a, p_a, \phi^K, p_{\phi^K})$, representing the symmetry reduced geometrodynamical phase space. The generalized momentum corresponding to the geometric degree of freedom is

$$p_a \equiv \frac{\delta \mathcal{L}}{\delta \dot{a}} = -\frac{6}{\kappa} a \dot{a}, \quad (2.7)$$

whereas conjugate momenta p_{ϕ^K} corresponding to the scalar field coordinates ϕ^K are

$$p_{\phi^K} = \frac{\delta \mathcal{L}}{\delta \dot{\phi}^K} = a^3 G_{KI} \dot{\phi}^I. \quad (2.8)$$

Now, using Legendre transformation and the inverse transformation, the symmetry reduced Hamiltonian \mathcal{H} for the multi-field scenario is immediately obtained as

$$\begin{aligned} \mathcal{H} &\equiv p_a \dot{a} + p_{\phi^I} \dot{\phi}^I - \mathcal{L}, \\ &= -\frac{\kappa p_a^2}{12a} + \frac{G^{LM}}{2a^3} p_{\phi^L} p_{\phi^M} + a^3 V(\phi^K), \end{aligned} \quad (2.9)$$

where we have used Eqs. (2.7) and (2.8).

The Hamilton's equations of motion can be expressed using the Poisson bracket formalism. The symplectic structure for the geometric and matter degrees of freedom are

$$\{a, p_a\} = 1, \quad (2.10a)$$

$$\{\phi^K, p_{\phi^K}\} = 1. \quad (2.10b)$$

With this information, the equation of motion for any phase space function, ξ , can be elegantly written as the Poisson flow of the quantity w.r.t the Hamiltonian:

$$\begin{aligned} \dot{\xi} &= \{\xi, \mathcal{H}\} \\ &= \left(\frac{\partial \xi}{\partial a} \frac{\partial \mathcal{H}}{\partial p_a} - \frac{\partial \xi}{\partial p_a} \frac{\partial \mathcal{H}}{\partial a} \right) + \left(\frac{\partial \xi}{\partial \phi^K} \frac{\partial \mathcal{H}}{\partial p_{\phi^K}} - \frac{\partial \xi}{\partial p_{\phi^K}} \frac{\partial \mathcal{H}}{\partial \phi^K} \right). \end{aligned} \quad (2.11)$$

Thus, the generic equations of motion for the phase space of a multi-field scenario in FLRW background are

$$\dot{a} = -\frac{\kappa p_a}{6a}, \quad (2.12a)$$

$$\dot{p}_a = -\frac{\kappa p_a^2}{12a^2} + \frac{3}{2a^4} G^{IJ} p_{\phi^I} p_{\phi^J} - 3a^2 V(\phi^K) \quad (2.12b)$$

$$\dot{\phi}^K = \frac{1}{a^3} G^{IK} p_{\phi^I}, \quad (2.12c)$$

$$\dot{p}_{\phi^K} = -a^3 V_{,K}(\phi^K) + \frac{1}{2a^3} G^{IP} G^{JQ} p_{\phi^I} p_{\phi^J} \frac{\partial G_{PQ}}{\partial \phi^K}. \quad (2.12d)$$

Evaluating the Poisson equations and using the Hamilton constraint, $\mathcal{H} = 0$, leads us to the Friedmann equations and the Klein-Gordon equations, consistent with those obtained via the Euler–Lagrange formalism. The Euler–Lagrange equations for this setup have been derived in the single-field case, which we extend here to the multi-field scenario. The equivalence of the two formulations, once again verifies the internal consistency.

The phase space under consideration is obtained through the symmetry reduction of the geometrodynamical variables (q_{ab}, p^{ab}) [1]. Since the spatial manifold in the flat FLRW model is non-compact, a fiducial flat metric ${}^o q_{ab}$ and a fiducial cell \mathcal{V} of coordinate volume V_o are introduced to regulate integrals [10]. The physical spatial metric is $q_{ab} = a^2 {}^o q_{ab}$, so that physical areas and lengths are obtained by scaling fiducial ones with appropriate powers of the scale factor [9, 10, 55].

To capture essential quantum geometric features in cosmology, one must construct symmetry-reduced models directly at the level of the connection-dynamics phase space, rather than in the original geometrodynamical setting [55, 56]. In the isotropic case, the triad variable is related to the scale factor via $|p| = a^2 V_o^{2/3}$ and $c = \gamma \dot{a} V_o^{1/3}$. Thus, for $V_o = 1$ the canonical pair $\{c, p\}$ is related to the scale factor a through [51, 55, 56]:

$$p = a^2, \quad c = \gamma \dot{a},$$

where c is the connection variable conjugate to the triad variable p , with γ denoting the Barbero–Immirzi parameter, commonly fixed as $\gamma = 0.2375$ [57, 58]. Thus, we transform the classical FLRW geometric phase space into a canonically equivalent connection dynamic phase space $\{c, p, \phi^K, p_{\phi^K}\}$, such that this transformation preserves the symplectic structure. In these variables, $\{c, p\} = \kappa\gamma/3$ [55, 59] and the Hamiltonian constraint takes the form:

$$\mathcal{H} = -\frac{3|p|^{1/2} c^2}{\kappa\gamma^2} + \frac{1}{2|p|^{3/2}} G^{IJ} p_{\phi^I} p_{\phi^J} + |p|^{3/2} V(\phi^K), \quad (2.13)$$

which is the standard starting point for LQC in the single field case and here extended to the multi-field.

Using the Poisson equation (2.11), we obtain the multi-field dynamics in the $c - p$ formulation:

$$\dot{c} = -\frac{c^2}{2\gamma|p|^{1/2}} - \frac{\kappa\gamma}{4|p|^{5/2}}G_{IJ}p_{\phi^I}p_{\phi^J} + \frac{\kappa\gamma}{2}|p|^{1/2}V, \quad (2.14a)$$

$$\dot{p} = \frac{2|p|^{1/2}c}{\gamma}, \quad (2.14b)$$

$$\dot{\phi}^I = \frac{1}{|p|^{3/2}}G^{IJ}p_{\phi^J}, \quad (2.14c)$$

$$\dot{p}_{\phi^I} = -|p|^{3/2}V_{,I} + \frac{1}{2|p|^{3/2}}G^{KP}G^{JQ}p_{\phi^K}p_{\phi^J}\frac{\partial G_{PQ}}{\partial\phi^I}. \quad (2.14d)$$

Thus, the complete connection dynamics for a generic multi scalar field matter source with minimal coupling to gravity for FLRW spacetime is contained in Eqs. (2.14a)–(2.14d).

The general theory of relativity does not admit a global notion of time, which is distinctly apparent in the canonical structure of the theory [3, 10, 60]. However, the requirement of an ‘‘agreed clock’’ demands that we consider the system in a relational way by treating one of the fields as the clock field, provided it satisfies the condition of monotonicity. Having said that, in the case of LQC, a massless scalar field serves this purpose, which later drives inflation upon the addition of a potential at the effective level. The situation, however, is distinct in our case: we have a non-trivial coupling of the scalar fields with the kinetic term specified by the field space metric G_{IJ} , making the energy density non-separable in terms of kinetic and potential contributions. This forbids switching off the potential term at the time of quantization. Since we want to construct a setup that is generic enough to allow all possibilities of interaction via G_{IJ} , we indeed require the introduction of an additional massless scalar field, Φ , to act as a clock field. This situation has already been encountered in Ref. [17].

B. Quantum Corrected Dynamics via Polymerization

In the FLRW background, the effective dynamics is obtained via the $\bar{\mu}$ polymerization scheme (improved dynamics) [10, 55, 59, 61] through the replacement:

$$c \longrightarrow \frac{\sin(\bar{\mu}c)}{\bar{\mu}},$$

where $\bar{\mu}$ encodes the edge length of the holonomy loop and is known as polymerisation parameter [17]. The holonomy loop encloses the minimum nonzero eigenvalue of area, namely the area gap Δ such that $\bar{\mu} = \sqrt{\frac{\Delta}{|p|}}$ [10] and $\Delta = 4\sqrt{3}\pi\gamma\ell_{\text{Pl}}^2$, where $\ell_{\text{Pl}} \equiv 1/m_{\text{Pl}}$ is the Planck length.

C. Background dynamics

We thus obtain the effective Friedmann, Raychaudhuri and Klein-Gordon equations, respectively, as given by

$$H^2 = \frac{\kappa\rho}{3} \left(1 - \frac{\rho}{\rho_c}\right), \quad (2.15a)$$

$$\frac{\ddot{a}}{a} = -\frac{\kappa\rho}{6} \left(1 - 4\frac{\rho}{\rho_c}\right) - \frac{\kappa P}{2} \left(1 - 2\frac{\rho}{\rho_c}\right), \quad (2.15b)$$

$$D_t\dot{\phi}^K + 3H\dot{\phi}^K + G^{IK}V_{,I} = 0. \quad (2.15c)$$

For later purposes, the Raychaudhuri equation (2.15b) can be rephrased as,

$$\dot{H}(t) = -\frac{\kappa}{2}(1 + \omega)\rho \left(1 - 2\frac{\rho}{\rho_c}\right). \quad (2.16)$$

Quantum geometry effects in LQC modify the effective Friedmann equation, Eq. (2.15a), such that the total energy density ρ attains a universal upper bound, the critical density ρ_c at the bounce, given by $\rho_c = 3/(\kappa\gamma^2\Delta)$ [10, 59]. At this point, the Hubble parameter vanishes, implying that the scale factor reaches a non-zero minimum and the cosmic contraction halts before transitioning into an expanding phase [12, 62].

The upper bound on the energy density arises strictly from holonomy corrections to the gravitational Hamiltonian and depends only on the total energy density, independent of the specific matter content [1, 13, 59]. Thus, even in multi-field scenarios, ρ is strictly bounded by ρ_c . From the energy density relation, Eq. (2.4), the critical value $\rho_c \approx 0.41m_{\text{Pl}}^4$ constrains the admissible values of the collective multi-field velocity $\dot{\sigma}$.

Finally, from the definition $\sigma^2 = G_{IJ}\dot{\phi}^I\dot{\phi}^J$, we obtain the effective Klein-Gordon equation for the adiabatic field σ as:

$$\ddot{\sigma} + 3H(t)\dot{\sigma} + V_{,\sigma} = 0. \quad (2.17)$$

Upon deriving the quantum-corrected equations, it becomes evident that the Klein-Gordon equation retains its classical form and does not receive any direct modifications from the holonomy corrections. The effects of quantum geometry enter only indirectly through the Hubble parameter $H(t)$ in the friction term, thereby influencing the field dynamics via the modified background evolution, as is the standard case in LQC in the single-field scenario [1–3].

Since the equations (2.15) are not independent, it suffices to solve the Klein-Gordon equations (2.15c) and the modified Friedmann equation (2.15a), as the Raychaudhuri equation (2.15b) follows from them and is thus redundant. We will focus on the two-field case such that $\phi^I = (\phi, \chi, \Phi)$ with an additional decoupled and globally monotonic relational clock field Φ .

Solving the autonomous system of coupled first and second order nonlinear equations yields the evolution of the dynamical variables $(a, \phi, \chi, \Phi, \dot{a}, \dot{\phi}, \dot{\chi}, \dot{\Phi})$, where

overdot denotes the derivative wrt cosmic time. Once these are specified, the system is completely determined and all other physically relevant quantities and cosmological parameters such as the energy density ρ , pressure density P , fractional energy density $\Omega \equiv \rho/\rho_c$ are constructed from them. In this framework, the scalar fields ϕ and χ drive the dynamics, while the scale factor a governs the cosmic expansion. To solve such a system numerically, an initial reference point in time is required, one that is necessarily traversed by this evolution. One of the physically motivated choice is the moment of the quantum bounce [33] (see, however, for example Refs. [29–31] and references therein for other physically motivated choice of taking initial conditions deep in the contracting phase). Since the scale factor can be freely rescaled without altering physical predictions, we fix $a = 1$ at the bounce without loss of generality, i.e., $a_B = a(t_B) = 1$.

In the Kinetic Energy Dominated (KED) bounce scenario, the universe typically evolves through three distinct phases: *the bounce, transition, and slow-roll* [63–69]. The evolution in this case displays a universal behavior that is largely insensitive to the specific choice of initial conditions and inflationary potentials, making the KED framework particularly advantageous for studying the pre-inflationary dynamics in multi-field models. In contrast, Potential Energy Dominated (PED) bounces can produce the desired slow-roll only under finely tuned initial configurations. Additionally, such cases generally lack the universal post-bounce dynamics characteristic of KED evolution. For a detailed study and comparison of the general features of pre-inflationary and inflationary phases in KED and PED bounces for a variety of single field models, we refer the reader to Ref. [67, 70, 71]. In this contribution, we restrict attention to the KED case.

To explore the sensitivity of the system to different initial conditions, we consider distinct initial values for one of the scalar fields, while that of the other fields are held the same for numerical analysis pertaining to the evolution of trajectories in both the models we will be analyzing. Additionally, variations in the initial value of the clock field Φ have no dynamical effect on the evolution equations and, as confirmed numerically, do not influence the dynamics of the system, being equivalent to a stiff fluid [17].

To analyze the behavior of dynamical variables and related quantities in the post-bounce inflationary phase, a few key parameters prove to be particularly useful. The evolution in the dominance of kinetic and potential energy largely governs these phases, making it essential to track their behavior through relevant indicators. Two such parameters are the equation of state parameter, $\omega \equiv P/\rho$, which represents the effective equation of state of the cosmic fluid represented by multiple scalar field system driving the dynamics and $r = \frac{KE}{PE}$, which represents the ratio of collective kinetic contribution of all fields to the collective potential energy [33, 72]. These parameters together help in identifying the distinct epochs within the pre-inflationary and inflationary phases and

provide an insight into the dominant form of energy at a given epoch.

During superinflation, where

$$\dot{H} > 0, \quad (2.18)$$

the equation of state satisfies $\omega > -1$, indicating a departure from standard slow-roll conditions in LQC [73]. Conversely, during the slow-roll inflationary phase, which is PED, the equation of state approaches $\omega \approx -1$. The parameter ω can further be expressed in terms of 'r' as $\omega = \frac{r-1}{r+1}$, revealing the conditions of 'r' that characterize the inflationary regime.

In addition, the two slow-roll parameters are defined as follows. The first Hubble slow-roll parameter, $\epsilon_H \equiv -\dot{H}/H^2$, measures the fractional rate of change of the Hubble parameter. The second multi-field Hubble slow-roll parameter, $\eta_H \equiv -\ddot{\sigma}/(H\dot{\sigma})$, measures whether the accelerated expansion can be sustained for sufficiently long period of time [74]. In the slow-roll regime, both parameters satisfy $\epsilon_H, \eta_H \ll 1$. These conditions ensure that the Hubble rate remains nearly constant during slow-roll inflation, leading to a prolonged, quasi-exponential expansion. Subsequently, the Hubble rate decreases more rapidly.

In LQC, the Friedmann equations (2.15) acquire quantum corrections due to which the behavior of ϵ_H and η_H can deviate from the standard predictions (i.e., in the usual GR case) and may lead to departures from the usual inflationary dynamics. In this context, it becomes important to examine the likelihood of occurrence of slow-roll inflation as well as generation of sufficient number of e-folds during this phase. The total number of e-folds, N_{inf} , is defined as usual by

$$N_{\text{inf}} = \ln\left(\frac{a_f}{a_i}\right) = \int_{t_i}^{t_f} H dt, \quad (2.19)$$

which quantifies the total exponential growth of the scale factor during the inflationary epoch. Here, subscript i refers to the scale factor at the beginning of the inflationary regime and f refers to end of inflation.

In the following, we present the two multi-field models that we will be analyzing in details in this work.

III. MODELS

We will present for two well-motivated multifield models:

A. Hybrid inflation

In hybrid inflation the potential is of the form [45]

$$V(\phi, \chi) = \frac{\lambda}{4}(\chi^2 - M^2)^2 + \frac{1}{2}m^2\phi^2 + \frac{1}{2}g^2\phi^2\chi^2, \quad (3.1)$$

where ϕ denotes the inflaton and χ is known as the waterfall field. Inflation proceeds as far as $\phi > \sqrt{\lambda}M/g$. The action is

$$S = \int d^4x \sqrt{-g} \left[\frac{R}{2\kappa} - \frac{1}{2}g^{\mu\nu} \partial_\mu \phi \partial_\nu \phi - \frac{1}{2}g^{\mu\nu} \partial_\mu \chi \partial_\nu \chi - \frac{1}{2}g^{\mu\nu} \partial_\mu \Phi \partial_\nu \Phi - \frac{\lambda}{4}(\chi^2 - M^2)^2 - \frac{1}{2}m^2\phi^2 - \frac{1}{2}g^2\phi^2\chi^2 \right]. \quad (3.2)$$

Here, the field space metric G_{IJ} with $\phi_1 = \phi$, $\phi_2 = \chi$ and $\phi_3 = \Phi$ is given by the trivial metric:

$$G_{IJ} = \begin{pmatrix} 1 & 0 & 0 \\ 0 & 1 & 0 \\ 0 & 0 & 1 \end{pmatrix}, \quad (3.3)$$

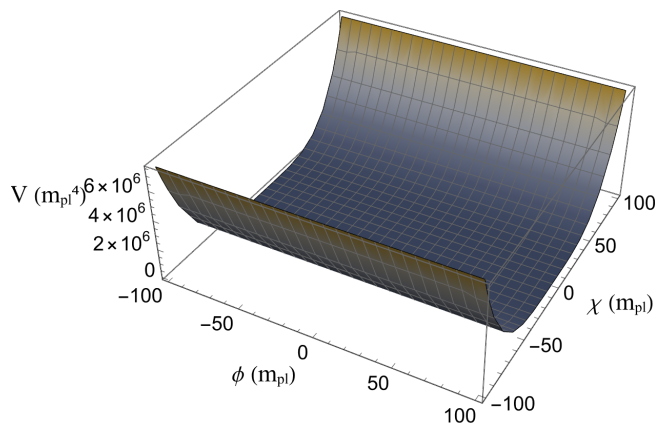


Figure 1. Potential profile of the hybrid potential model Eq. (3.1). This profile is evaluated for the parameter values $M = 1 m_{Pl}$, $\lambda = 0.3$, $g = 10^{-5}$, $m = 0.01 m_{Pl}$.

The quantum corrected Friedmann equations are given in Eqs. (2.15), (2.16). The Klein Gordon equations obtained from Eq. (2.15c) corresponding to all the component fields for this model are:

$$\ddot{\phi} + 3H\dot{\phi} + m^2\phi + g^2\chi^2\phi = 0, \quad (3.4)$$

$$S = \int d^4x \sqrt{-g} \left[\frac{R}{2\kappa} - \frac{1}{2}g^{\mu\nu} \partial_\mu \phi \partial_\nu \phi - \frac{e^{2b(\phi)}}{2}g^{\mu\nu} \partial_\mu \chi \partial_\nu \chi - \frac{1}{2}g^{\mu\nu} \partial_\mu \Phi \partial_\nu \Phi - \frac{1}{2}m^2\phi^2 - \frac{1}{2}g^2\phi^2\chi^2 \right]. \quad (3.9)$$

Note that here we have an explicit kinetic coupling of ϕ with χ . The scalar field ϕ here makes the role similar to the dilaton in string-inspired models (e.g. like in heterotic string models [75]).

Here, the field space metric G_{IJ} with $\phi_1 = \phi$, $\phi_2 = \chi$

$$\ddot{\chi} + 3H\dot{\chi} + g^2\phi^2\chi + \lambda\chi(\chi^2 - M^2) = 0, \quad (3.5)$$

$$\ddot{\Phi} + 3H\dot{\Phi} = 0. \quad (3.6)$$

The hybrid potential naturally exhibits a symmetry-breaking structure in which the system initially evolves along a symmetric valley with $\chi = 0$ for sufficiently large values of ϕ . In this regime, the discrete symmetry remains unbroken and the potential energy is approximately constant, dominated by the vacuum energy of the χ sector. As the inflaton rolls down its potential, the value of ϕ decreases. When the inflaton field drops below the critical value ϕ_c given by,

$$\phi_c = \frac{\sqrt{\lambda}}{g}M, \quad (3.7)$$

the effective mass becomes negative, the χ field becomes tachyonic and undergoes a rapid *waterfall transition* towards one of the degenerate symmetry-broken vacua $\chi = \pm M$. The vacuum structure of the theory is therefore determined by the minima of the potential along the χ direction. This mechanism provides a natural dynamical end to inflation and determines the vacuum structure of the model.

B. String-inspired model

The second model we will analyze is characterized by the potential

$$V(\phi, \chi) = \frac{1}{2}m^2\phi^2 + \frac{1}{2}g^2\phi^2\chi^2, \quad (3.8)$$

with the action

and $\phi_3 = \Phi$ is given by the non-trivial metric:

$$G_{IJ} = \begin{pmatrix} 1 & 0 & 0 \\ 0 & e^{2b(\phi)} & 0 \\ 0 & 0 & 1 \end{pmatrix}, \quad (3.10)$$

The kinetically coupled multi-field action, character-

ized by a hyperbolic field-space structure [41] as indicated by the scalar field metric G_{IJ} , represents the next string-inspired model. In this framework, the field $\phi_1 = \phi$ acts as the inflaton, decaying into the field $\phi_2 = \chi$ and $\phi_3 = \Phi$ serves as a clock.

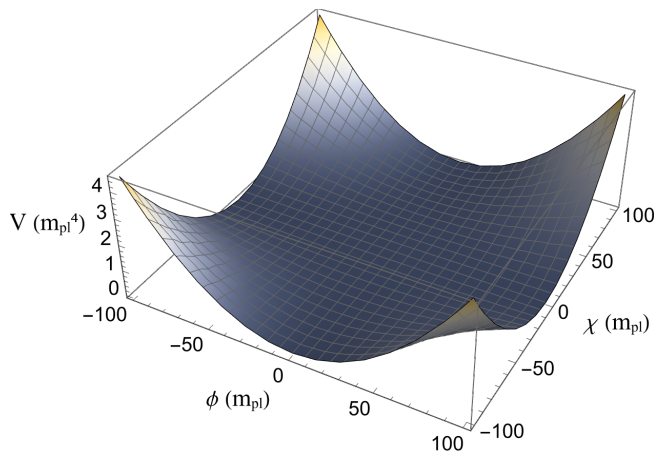


Figure 2. Potential profile of the string-inspired model Eq. (3.8). The parameters are assumed to be: $m = 10^{-6} m_{Pl}$ and $g = 3 \times 10^{-4}$.

For the field space metric (3.10), we choose $b(\phi) = \beta\phi$, with β an arbitrary constant [41, 76].

For this setup, the Klein Gordon equations are:

$$\ddot{\phi} + 3H(t)\dot{\phi} - \beta e^{2\beta\phi}\dot{\chi}^2 + m^2\phi + g^2\chi^2\phi = 0 \quad (3.11a)$$

$$\ddot{\chi} + 3H(t)\dot{\chi} + 2\beta\dot{\phi}\dot{\chi} + e^{-2\beta\phi}g^2\phi^2\chi = 0, \quad (3.11b)$$

$$\ddot{\Phi} + 3H(t)\dot{\Phi} = 0. \quad (3.11c)$$

The quantum corrected Friedmann equations can again be referred back to equations (2.15a) and (2.16) In the next two sections, we present the detailed analysis for each of the two models specified above.

IV. BACKGROUND DYNAMICS FOR THE HYBRID INFLATION

A. Numerical analysis

The pre-inflationary and inflationary LQC epochs evolved for this model from KED bounce are listed in the Table XII.

The resulting background evolution is illustrated in Fig. 3. Numerically, as seen in Fig. 3a, the scale factor a remains stationary at the bounce, with both its time derivative and the Hubble parameter H vanishing. Although all trajectories start from identical initial conditions at the bounce, their subsequent evolution diverges depending on the specific initial values; nevertheless, the qualitative behavior is consistent across trajectories, confirming the robustness of the underlying dynamical mechanisms.

Quantum bounce is immediately followed by superinflation which is defined by the condition (2.18), corresponding to a rapid increase in the Hubble parameter. From the modified Friedmann equation in LQC (2.16), quantum corrections alter the classical dynamics: since the kinetic term $(\rho + P)$ remains positive, superinflation requires the correction factor $(1 - 2\frac{\rho}{\rho_c})$ to be negative. This leads to the conditions: $\rho > \frac{\rho_c}{2}, \omega > -1$, which delineate the superinflationary phase. In contrast, classical GR would require a violation of the Null Energy Condition for superinflation in Eq. (2.3b), since (2.18) would imply negative kinetic energy [78].

At the end of superinflation, $\dot{H} \rightarrow 0$, consistent with the observations in Fig. 3b and Fig. 4a. During this transition, the inflaton loses kinetic energy and the pressure begins to decrease, signaling the onset of a potential-dominated damping region. For all the initial field values $\phi_B = \{1, 2, 3\}m_{Pl}$, the end of superinflation occurs at the same epoch $t = 0.239 m_{Pl}^{-1}$, refer Table I.

We identify the onset of the slow-roll phase by the condition $\omega = -1/3$, see I. From the Raychaudhuri equation (2.15b), neglecting the quantum correction terms, it follows that $\ddot{a} > 0$ precisely when $\rho + 3P < 0$, i.e. $\omega < -1/3$. In this LQC numerical evolution, the classical criterion is applied once the dynamics are sufficiently far from the bounce that is when the total energy density has decreased to a fraction of the critical density and quantum corrections become negligible so that the classical Friedmann relations hold to a good approximation.

Consequently, the universe undergoes continuous accelerated expansion: initially super-exponentially immediately after the bounce, and then in a sustained slow-roll phase. This sustained acceleration during slow-roll is further corroborated by the observations in Fig. 3, where the scale factor a and its time derivative \dot{a} exhibit nearly exponential growth, the Hubble parameter H remains approximately constant and its derivative \dot{H} , Fig. 3b is negative but very small, consistent with slow-roll dynamics.

The clock field in Fig. 5 remains stationary at a small value determined by the initial conditions. In the hybrid inflation model, characterized by III A, the post-bounce dynamics of the component fields can be directly understood from the coupled Klein-Gordon equations (3.6) alongside the modified Friedmann equations in LQC (2.15a). Starting with the critical value ρ_c , with $H = 0$ and $\dot{H} > 0$ at the KED bounce, the total energy density decreases as $\dot{\rho} = -3H(\dot{\phi}^2 + \dot{\chi}^2 + \dot{\Phi}^2) < 0$, as the fields are eventually slowed by expansion in Fig. 6a.

To analyze the stability of the χ field, one considers its effective mass squared, defined as the curvature of the potential along the χ direction,

$$m_{\chi,\text{eff}}^2(\phi, \chi) = \frac{\partial^2 V}{\partial \chi^2} = g^2\phi^2 + \lambda(3\chi^2 - M^2). \quad (4.1)$$

This expression shows that in the full multi-field configuration space, the effective mass depends on both ϕ and

Epoch	Condition	$\phi_B = 1 m_{Pl}$	$\phi_B = 2 m_{Pl}$	$\phi_B = 3 m_{Pl}$
End of superinflation	$\rho = 0.205 m_{Pl}^4$	0.239	0.239	0.239
KE=PE	$\omega = 0$	0.340	0.339	0.339
Onset of slow-roll	$\omega = -1/3$	0.474	0.474	0.472
End of slow-roll	$\omega = -1/3$	26.11	26.17	26.27
$\log a_{\text{initial}}$	—	0.3648	0.3648	0.3632
$\log a_{\text{final}}$	—	17.0846	17.1023	17.131
e-folds (N_{inf})	$\log a_f - \log a_i$	16.7198	16.7375	16.7678

Table I. Characteristic epochs of the quantum corrected background evolution for the hybrid potential model 1, determined from the corresponding diagnostic criteria. The listed epochs are in Planck units (m_{Pl}^{-1}) [77].

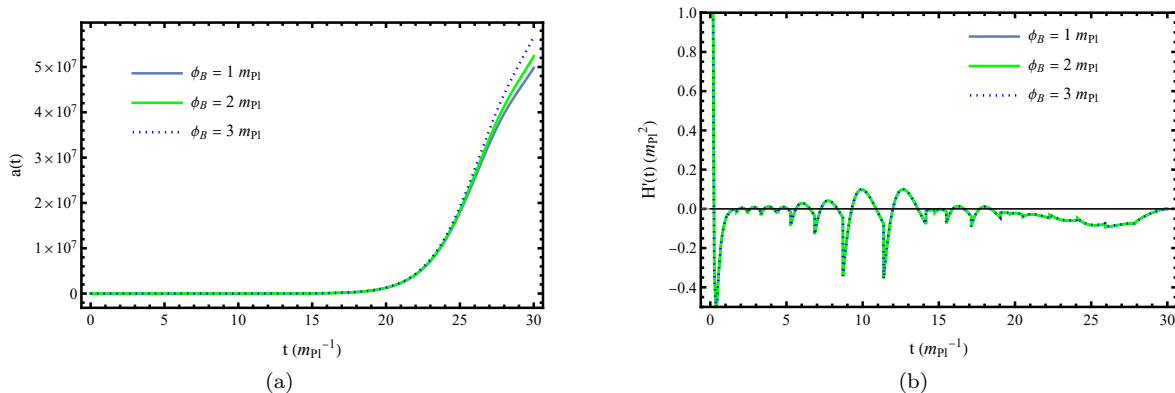


Figure 3. Evolution of (a) the scale factor $a(t)$, and (b) $H(t)$ for the Linde's hybrid potential model 1 with a canonical kinetic space represented by the metric 3.3, in the LQC framework. The χ_B value is fixed at $0.01 m_{Pl}$ and its velocity $\dot{\chi}_B = 0.05 m_{Pl}^2$. The initial values of clock field and its velocity are fixed at $(\Phi_B, \dot{\Phi}_B) = (0.5 m_{Pl}, 0.5 m_{Pl}^2)$. The initial values of the field ϕ are taken as 1, 2, and 3 m_{Pl} , the model parameters are $m = 0.01 m_{Pl}$, $g = 10^{-5}$, $M = 1 m_{Pl}$, $\lambda = 0.3$ which are consistently used throughout this analysis. These plots highlight the modifications introduced by quantum gravitational corrections compared to the classical dynamics.

χ . However, during the inflationary phase, the system evolves approximately along the valley $\chi = 0$. Evaluating the above expression along this trajectory gives

$$m_{\chi, \text{eff}}^2(\phi) = g^2 \phi^2 - \lambda M^2. \quad (4.2)$$

The sign of this quantity determines the stability of the χ direction. Evaluating it for $\phi_B = \{1, 2, 3\} m_{Pl}$, we obtain $m_{\chi, \text{eff}}^2(\phi_B) \approx -0.3 m_{Pl}^2$ at bounce. The critical value of the inflaton given by Eq. (3.7) at which the waterfall instability sets in is $\phi_c \approx 5.48 \times 10^4 m_{Pl}$. Since the initial inflaton values satisfy $\phi_B = \{1, 2, 3\} m_{Pl} \ll \phi_c$, the system begins its evolution already inside the tachyonic regime.

The true vacuum of the potential is obtained by minimizing the potential with respect to both the scalar fields, which yields $(\phi, \chi) = (0, \pm M) = (0, \pm 1 m_{Pl})$, $V = 0$ as the global minima of the potential. In contrast, the point $(\phi, \chi) = (0, 0)$ corresponds to a local maximum along the χ direction with $V(0, 0) = \frac{\lambda M^4}{4} = 0.075 m_{Pl}^4$ and therefore represents a false vacuum state.

Soon after the KED bounce, the dynamics are dominated by the kinetic energy of the scalar fields. As the universe expands, Hubble friction rapidly dilutes these kinetic contributions, while the false vacuum energy given

by $V(0, 0) = 0.075 M_{Pl}^4$ remains constant, see Fig. 7a. Once the kinetic energy becomes subdominant, the total energy density is effectively controlled by this vacuum contribution, leading to an approximately constant Hubble rate determined by $H^2 \simeq \frac{\kappa V(0, 0)}{3} (1 - \frac{V(0, 0)}{\rho_c})$ and thus primarily driving slow-roll instead of it being driven by the flatness of the inflaton potential alone.

Although the system is already in the tachyonic regime, the actual evolution of the waterfall phase is governed by the competition between the tachyonic instability and Hubble damping. This can be quantified by comparing the instability scale $|m_{\chi}^2|$ to the Hubble scale H^2 [79, 80].

For the parameter values considered in this case, this comparison places the model in a mildly fast waterfall regime, in which the tachyonic instability is faster than the Hubble expansion but not instantaneous. Consequently, inflation does not terminate immediately after the onset of the instability. Instead, a non-negligible fraction of inflation occurs while the system evolves along the waterfall trajectory [81].

In this regime, the duration of inflation is controlled not by the critical point ϕ_c , but by the time required for the waterfall field χ to grow sufficiently large to end vacuum domination.

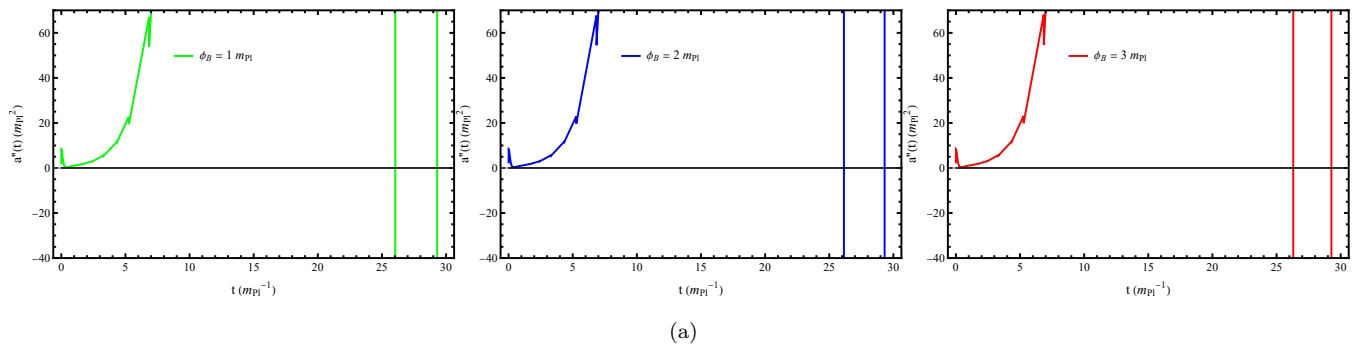


Figure 4. Each panel corresponds to the plot of $\ddot{a}(t)$ for different values of ϕ_B in the hybrid model 1 within the LQC framework, with model parameters and initial conditions identical to those in Fig. 3. It can be clearly seen that the acceleration $\ddot{a}(t)$ remains positive throughout the slow-roll phase.

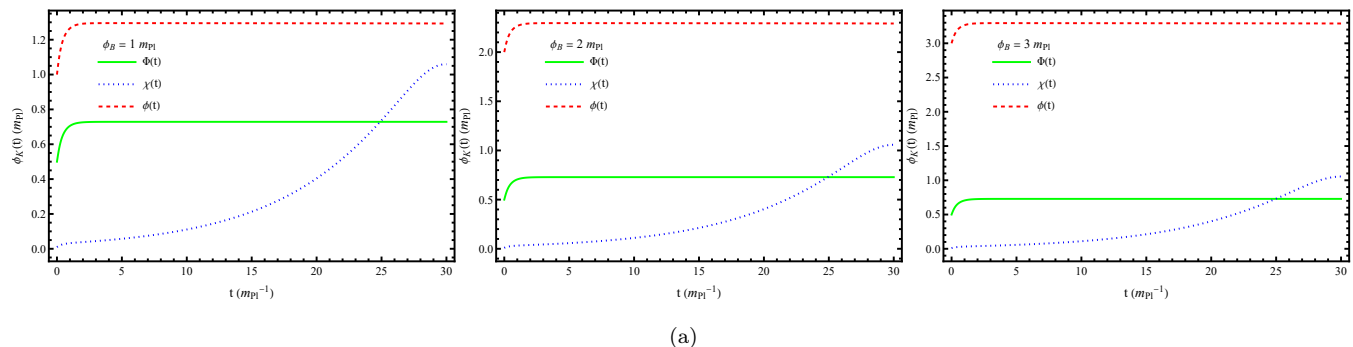


Figure 5. Evolution of the component fields $\phi(t)$, $\chi(t)$ and $\Phi(t)$ for the hybrid potential model 1 in the LQC framework. Each panel, corresponding to a distinct value of ϕ_B , illustrates the dynamics of the fields from bounce onwards. The clock field $\Phi(t)$ remains constant throughout the evolution, unaffected by the dynamical interactions.

During this phase, the tachyonic growth of the waterfall field induces transient features in the background dynamics. As χ begins to grow, Fig. 5, a portion of the vacuum energy is converted into kinetic energy, leading to temporary increase in $\dot{\chi}^2$, Fig. 6. This produces corresponding fluctuations in \dot{H} , even though the background remains in an overall slow-roll inflationary state.

From Fig. 7a, as the total energy density decreases, the kinetic energy drops much more rapidly than the potential energy. This is because, during the damping region, the Hubble friction term in $\dot{K}E = -3H\dot{\sigma}^2 - \dot{\sigma}V'(\sigma)$ continues to dominate, thereby driving the transition into PED phase. During the slow-roll phase, the change in kinetic energy is nearly zero while the change in potential energy is very slow.

Using the identity $\omega = \frac{r-1}{r+1}$, the condition $\omega > -1$ implies that $r > 0$, as is also apparent in Figs. 8a, 8b that $r > 1$, confirming that kinetic energy dominates over potential energy throughout superinflation. This is consistent with the expected evolution from a KED phase at the bounce into the superinflationary regime, which persists until the energy density decreases to half its critical value $0.205 m_{Pl}^4$. The characteristics and duration of this superinflationary phase are highly sensitive to the potential parameters and initial conditions (see, e.g. ref. [73]).

Soon after the superinflation ends, at $t = 0.340 m_{Pl}^{-1}$, $t = 0.339 m_{Pl}^{-1}$ and $t = 0.339 m_{Pl}^{-1}$, see Table I, we have $\omega = 0$ and $r = 1$ for $\phi_B = 1 m_{Pl}$, $\phi_B = 2 m_{Pl}$ and $\phi_B = 3 m_{Pl}$, respectively, refer Figs. 8a, 8b, indicating that the kinetic and potential energies are equal. Before this point, r decreases rapidly during transition as the kinetic energy dilutes, until the universe eventually enters the PED damping region. Ultimately, irrespective of the initial values, we can observe $\omega \approx -1$ and $r \ll 1$ in Fig. 8 indicating the slow-roll phase.

During the superinflationary phase, $\epsilon_H < 0$ since $\dot{H} > 0$. At epoch $t = 0.239 m_{Pl}^{-1}$ for all of $\phi_B = \{1, 2, 3\} m_{Pl}$, see Table I, ϵ_H transitions from negative to positive values, marking the end of superinflation, as seen in Fig. 9a. This timing is consistent with the behavior observed in the previous plots. Beyond this point, the system enters the damping region, after which the first slow-roll parameter remains $\epsilon_H \ll 1$ during the slow-roll regime. From the second slow-roll parameter in Fig. 9b, one finds that η_H also approaches its maximum value around the same epochs and subsequently decreases, eventually settling to $\eta_H \ll 1$ as the slow-roll phase is approached, in agreement with expectations.

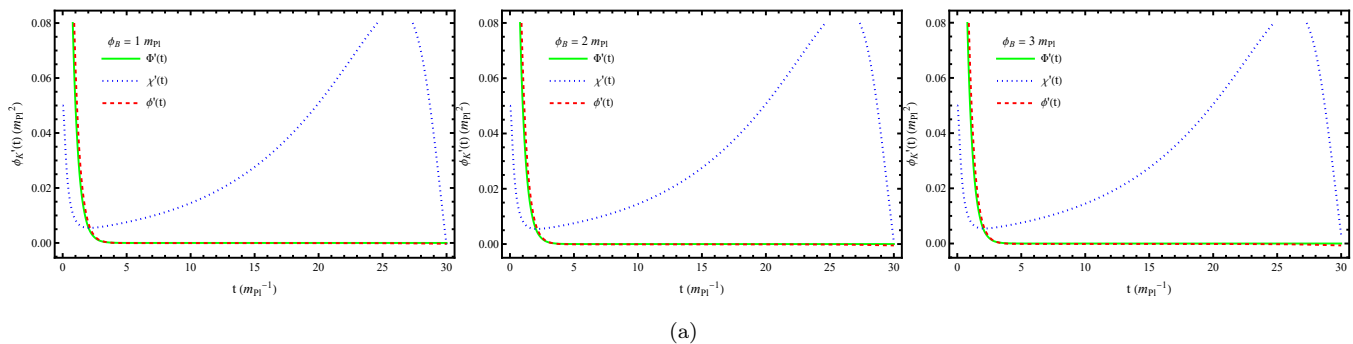


Figure 6. Each panel, corresponding to a distinct value of ϕ_B , depicts the evolution of the field velocities $\dot{\phi}(t)$, $\dot{\chi}(t)$ and $\dot{\Phi}(t)$ for the hybrid potential model 1.

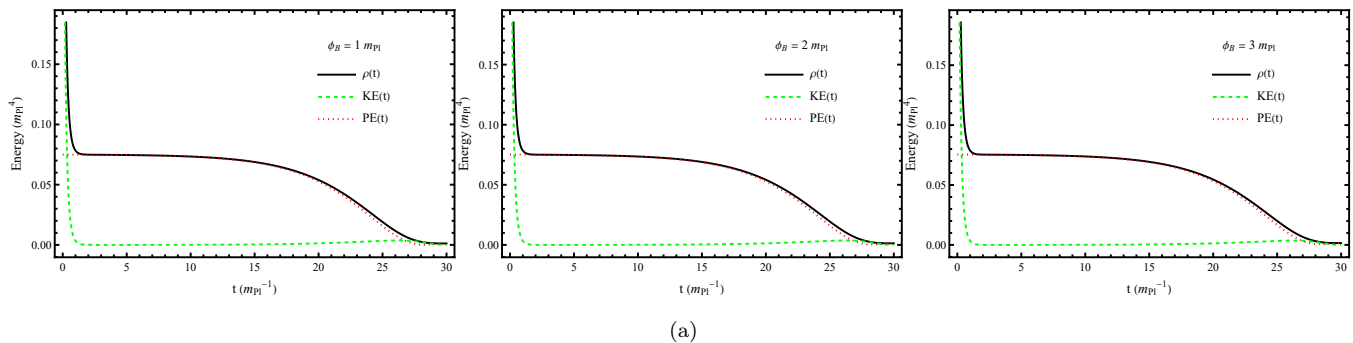


Figure 7. Comparison of the kinetic energy, potential energy, and total energy density during the pre-inflationary evolution of the hybrid model 1. Each panel corresponds to a distinct initial value ϕ_B . The potential energy gradually overtakes the total energy density during the slow-roll phase as the kinetic energy rapidly declines, signaling the onset of potential-energy domination and sustained inflation.

The slow-roll phase, which begins at $t = 0.474 m_{Pl}^{-1}$ for all of $\phi_B = \{1, 2, 3\} m_{Pl}$, see I, the kinetic contribution is subdominant relative to the potential, so the pressure effectively reduces to $P \simeq -V(\phi, \chi)$, giving rise to the PED negative-pressure sustained slow-roll region Fig. 10a.

As the universe enters the expanding branch ($H > 0$), both fields experience Hubble friction, but their initial velocities determine the direction of motion in field space. We begin by examining the configuration in which both the inflaton and auxiliary scalar fields emerge from the quantum bounce with positive initial velocities, i.e. $\dot{\phi}_B > 0$ and $\dot{\chi}_B > 0$.

As shown in Table II, quantitatively sweeping ϕ_B from 0.001 to $8 m_{Pl}$ while keeping χ_B fixed leads to a monotonic increase in the inflationary duration and changes N_{inf} calculated using Fig. 10b, only mildly, from approximately 16.6 to 17.7, showing that the e-fold count quickly saturates at relatively small values of ϕ_B and exhibits little further enhancement thereafter. The complementary variation with respect to the auxiliary field χ_B , presented in Table III, reveals a much stronger sensitivity as χ_B increases from 10^{-5} to $0.4 m_{Pl}$, N_{inf} drops sharply from about 18.7 down to nearly 2.6. This demonstrates that the auxiliary field amplitude acts as a controlling thresh-

old parameter for the success of inflation, since small variations in its initial value significantly alter the time the trajectory remains within the inflationary valley, thereby determining whether sufficient e-folds are generated. In both field directions of variations in bounce values, the values below the lower extremes of these ranges show saturation in N_{inf} , while values above the upper extremes fail to achieve a sustained slow-roll valley before sufficient e-folds accumulate. These trends are visually confirmed in Fig. 11, where both dependencies produce smooth and monotonic curves.

Since the bounce occurs in a KED regime, the fields initially evolve in a superinflationary phase due to quantum correction effects. Although $\phi_B < \phi_c$, inflation can still occur if the tachyonic growth of the auxiliary field is sufficiently slow to allow the vacuum energy to dominate. Increasing ϕ_B makes the effective tachyonic mass less negative, thereby weakening the instability and delaying the growth of the auxiliary field. This extends the time required for χ to reach the true vacuum value and consequently leads to a mild increase in the number of e-folds. In contrast, a larger initial auxiliary field amplitude χ_B enhances the instability during the KED phase, causing the system to reach the true vacuum more rapidly and reducing the duration of inflation.

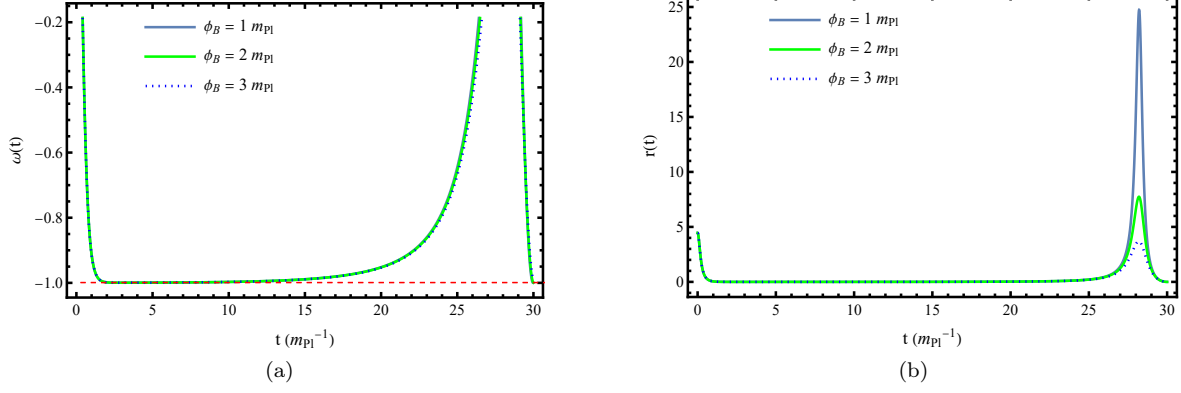


Figure 8. Evolution of (a) the equation-of-state parameter $\omega(t)$ and (b) the kinetic-to-potential energy ratio $r(t)$ for the hybrid potential model 1 in the LQC framework. The red dashed line marks $\omega = -\frac{1}{3}$, indicating the threshold for the onset and termination of the slow-roll phase. A smooth transition is observed from ($\omega \approx +1$) to ($\omega \approx -1$). The slow-roll phase concludes as ω rises above $-\frac{1}{3}$. Both panels consistently demonstrate a finite, successful, and PED inflationary regime.

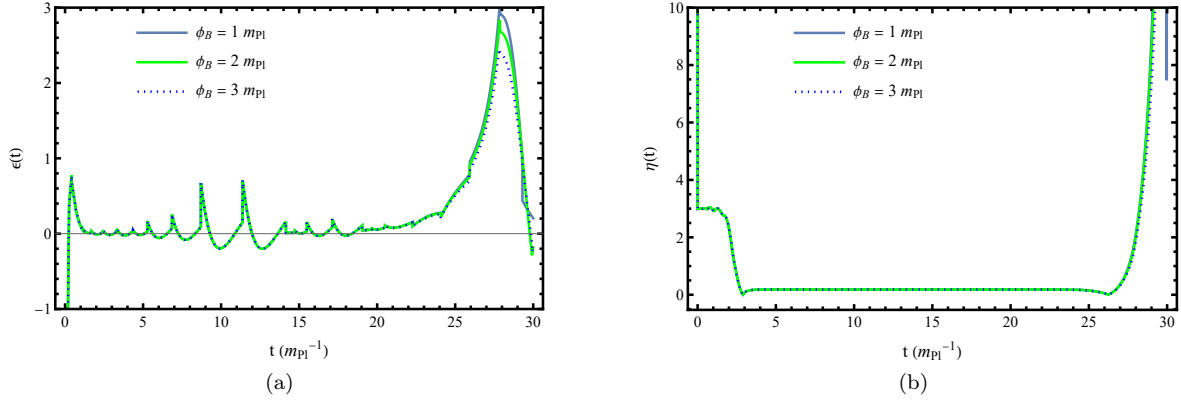


Figure 9. Evolution of the slow-roll parameters (a) $\epsilon_H(t)$ and (b) $\eta_H(t)$ for the hybrid potential model 1 in the LQC framework. These plots illustrate the onset and the end of slow-roll phase. Both $\epsilon_H, \eta_H \ll 1$ during the regime, while $\epsilon_H < 0$ during superinflation.

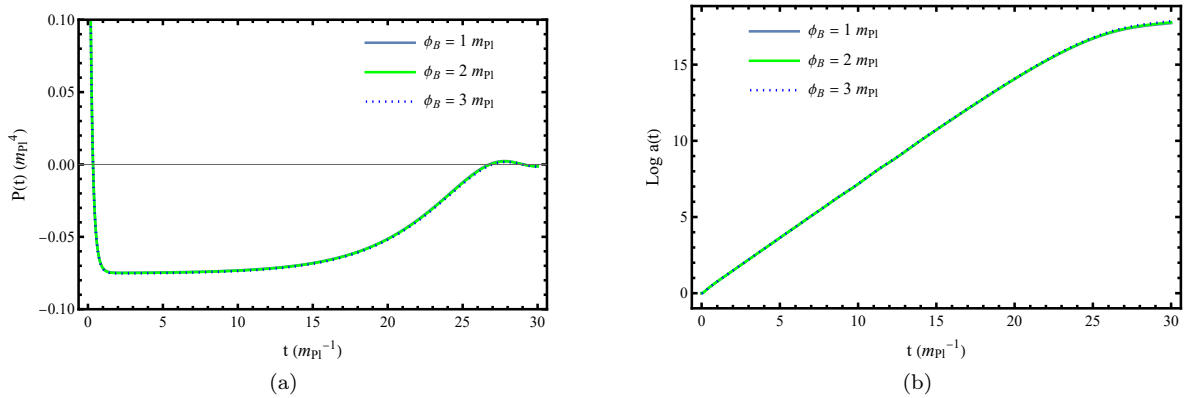


Figure 10. The above figure shows the evolution of (a) the pressure and (b) $\log a(t)$ for the hybrid potential model 1 in the LQC framework. The pressure transitions to negative values as the system enters the slow-roll regime and remains negative throughout this phase, consistent with the conditions required for accelerated expansion.

$\phi_B (m_{\text{Pl}})$	$t_{\text{start}} (m_{\text{Pl}}^{-1})$	$t_{\text{end}} (m_{\text{Pl}}^{-1})$	$\ln(a_i)$	$\ln(a_f)$	N_{inf}
0.001	0.47281	26.081	0.363861	17.0626	16.698
0.01	0.47279	26.08398	0.363845	17.0635	16.699
0.1	0.472785	26.08531	0.363847	17.0645	16.700
0.5	0.472794	26.09388	0.363863	17.071	16.707
1	0.47265	26.114	0.36374	17.0858	16.722
2	0.47216	26.179	0.363366	17.1823	16.818
3	0.47111	26.285	0.362496	17.214	16.851
4	0.47000	26.433	0.361593	17.3221	16.960
5	0.46831	26.635	0.360211	17.4632	17.102
6	0.50000	26.900	0.386412	17.6398	17.253
8	0.50000	27.900	0.386549	18.1704	17.783

Table II. Number of e-folds N_{inf} for varying initial values of ϕ_B with $\dot{\phi}_B > 0$ and $\dot{\chi}_B > 0$. The bounce value of the auxiliary field is fixed at $\chi_B = 0.01 m_{\text{Pl}}$, while the clock field satisfies $\Phi_B = 0.5 m_{\text{Pl}}$ with $\dot{\chi}_B = 0.05 m_{\text{Pl}}^2$ and $\dot{\Phi}_B = 0.5 m_{\text{Pl}}^2$. The value of $\dot{\phi}_B$ is then computed using energy density constraint. The model is computed with $m_{\text{Pl}} = 1$, $\rho_c = 0.41 m_{\text{Pl}}^4$, $m = 0.01 m_{\text{Pl}}$, $g = 10^{-5}$, $M = 1 m_{\text{Pl}}$, $\lambda = 0.3$, and $\beta = 0$. Thus, the field-space metric is trivial, $G_{IJ} = \delta_{IJ}$.

$\chi_B (m_{\text{Pl}})$	$t_{\text{start}} (m_{\text{Pl}}^{-1})$	$t_{\text{end}} (m_{\text{Pl}}^{-1})$	$\ln(a_i)$	$\ln(a_f)$	N_{inf}
10^{-5}	0.50	29.0	0.386215	19.1353	18.7490
10^{-4}	0.50	28.9	0.386209	18.9983	18.6120
10^{-3}	0.50	28.6	0.386216	18.8747	18.4884
10^{-2}	0.473	26.07	0.364019	17.0594	16.6953
10^{-1}	0.509	15.75	0.370476	9.67541	9.3049
0.2	0.61	11.07	0.387649	6.34551	5.9578
0.3	0.57	8.36	0.416632	4.57032	4.1536
0.4	0.71	6.22	0.457536	3.15351	2.6959

Table III. Number of e-folds N_{inf} for varying initial values of χ_B with $\dot{\phi}_B > 0$ and $\dot{\chi}_B > 0$. The inflaton bounce value is fixed at $\phi_B = 0.01 m_{\text{Pl}}$ and $\dot{\phi}_B$ is then computed using energy density constraint. All the other initial values and model parameters are kept same as in Table II for consistency in comparison and analysis.

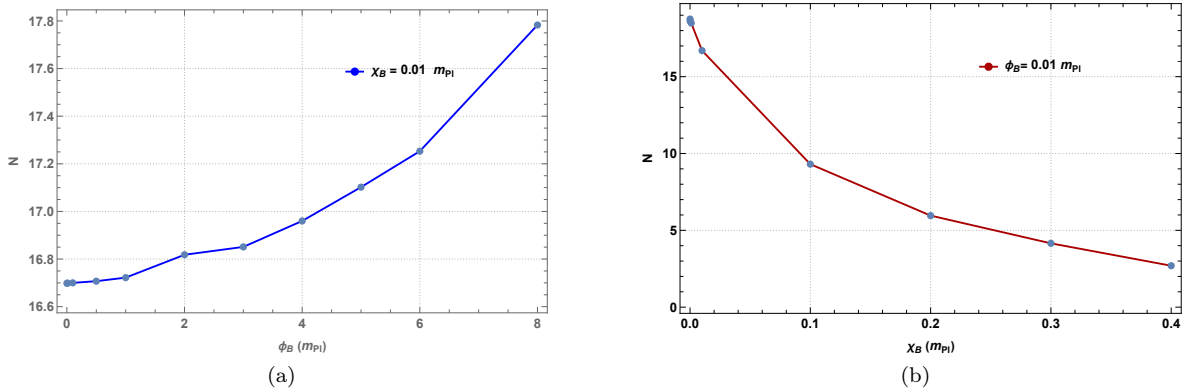


Figure 11. (a) Variation of the number of e-folds N_{inf} with respect to the initial value ϕ_B for a fixed $\chi_B = 0.01 m_{\text{Pl}}$. (b) Variation of the number of e-folds N_{inf} with respect to the initial value χ_B for fixed value of $\phi_B = 0.01 m_{\text{Pl}}$. The panels correspond to $\dot{\phi}_B > 0$ and $\dot{\chi}_B > 0$, i.e., both field velocities are positive at the bounce.

$\phi_B (m_{\text{Pl}})$	$t_i (m_{\text{Pl}}^{-1})$	$t_f (m_{\text{Pl}}^{-1})$	$\ln a_i$	$\ln a_f$	N_{inf}
0.001	0.48	33.65	0.369811	22.4846	22.1148
0.01	0.476	33.65	0.366511	22.4846	22.1181
0.1	0.474	33.65	0.364864	22.4842	22.1193
1	0.47	33.64	0.361553	22.486	22.1244
2	0.48	33.70	0.369831	22.5299	22.1601
4	0.47	33.93	0.361585	22.7146	22.3530
6	0.47	33.65	0.361548	22.4846	22.1231
8	0.48	19.20	0.369768	12.1489	11.7791
10	0.64	5.39	0.478037	2.711	2.2330

Table IV. Number of e-folds N_{inf} for varying initial values of ϕ_B with $\dot{\phi}_B < 0$ and $\dot{\chi}_B < 0$. The bounce value of the auxiliary field is fixed to $\chi_B = 0.01 m_{\text{Pl}}$ and ϕ_B is then computed using energy density constraint. All the other initial values and model parameters are kept same as in Table II.

In contrast, the case in which both fields begin with negative initial velocities, $\dot{\phi}_B < 0$ and $\dot{\chi}_B < 0$, exhibits significantly different behaviour. Table IV shows that varying ϕ_B produces large N_{inf} only when the initial amplitude is small. Once the inflaton amplitude grows beyond $\sim 6 m_{\text{Pl}}$, the system shows significant decline in the total e-folds. A similar trend is observed when varying χ_B in Table V where even moderate increases in χ_B sharply reduce the duration of inflation.

The third scenario corresponds to mixed initial velocities, with $\dot{\phi}_B < 0$ and $\dot{\chi}_B > 0$. As seen in Table VI, varying ϕ_B in this case results in only modest changes in N_{inf} , with the e-folds remaining relatively stable over a wide range of initial amplitudes. The inflationary phase in this case 13 shows similar trend and range as in the fully positive initial velocities case. The variation with respect to χ_B (Table VII) again produces a monotonic decline in N_{inf} as χ_B increases.

In the remaining mixed case with $\dot{\phi}_B > 0$ and $\dot{\chi}_B < 0$, varying ϕ_B leads to only small changes in N_{inf} , while sweeping χ_B produces large declines in inflation duration. A quantitative examination of the e-fold ranges highlights the asymmetry in sensitivity between the inflaton and the auxiliary field. Sweeping χ_B across its allowed range produces large changes in N_{inf} in every configuration. By contrast, sweeping ϕ_B changes the total e-folds by less than 1.1 in three of the four cases, indicating that N_{inf} saturates rapidly once ϕ_B exceeds a small threshold. The single exception is the fully negative configuration, where large ϕ_B drives the trajectory away from the slow-roll region. In other words, χ_B effectively sets the conducive condition for whether slow-roll is achieved, whereas ϕ_B mostly regulates how long inflation lasts once it is reached.

A key global observation is that, for the parameter values chosen in this study, none of the configurations yield the canonical $N_{\text{inf}} \gtrsim 60$ e-folds required for observational consistency in standard cosmology. Successful long-duration inflation in the Linde hybrid model in LQC therefore likely requires either carefully tuned initial data or choices of coupling parameters.

From Table X, we observe that for KED bounce, the model consistently yields a slow-roll inflationary phase

with approximately 60 e-folds of hybrid inflation before the waterfall transition is reached, for suitable parameter choices following the Ref. [82]. The highlighted rows indicate representative initial conditions for which $N_{\text{inf}} \simeq 60$ is achieved. This demonstrates that by appropriately fine-tuning the initial phase space variables at the bounce, the model remains viable within the LQC framework irrespective of the sign of the initial field velocities.

The number of e-folds of expansion during the pre-inflationary phase, across the scanned phase space and for all configurations of the initial velocity signs is $N_{\text{preinf}} \approx 0.2 - 0.4$. This indicates that the pre-inflationary regime contributes only a very small amount to the total expansion of the universe, with the dominant growth occurring during the subsequent slow-roll inflationary phase.

For completeness, the analytical background solutions corresponding to the bounce, superinflationary, and slow-roll phases are presented in Appendix A. These derivations provide explicit expressions for the field, scale factor, and Hubble evolution under the same approximations employed in the numerical analysis, allowing a direct comparison between the analytical and numerical treatments of the model. These solutions are evaluated in terms of the adiabatic field σ , rather than the individual field components, to capture the collective inflationary dynamics of the system.

B. Qualitative Analysis: Dynamical System Approach

By recasting the modified Friedmann Eq. (2.15) and Klein-Gordon equations (3.6) for our chosen configuration of potential and G_{IJ} metric (3.3) into an autonomous system of first-order differential equations, whose critical points determine the asymptotic cosmological behavior and allow a stability analysis. In order to do so, we define a set of dimensionless dynamical variables that normalize the fields' kinetic energies, components of potential energy and the relative energy density. Thus, the definitions of dynamical variables are adapted from

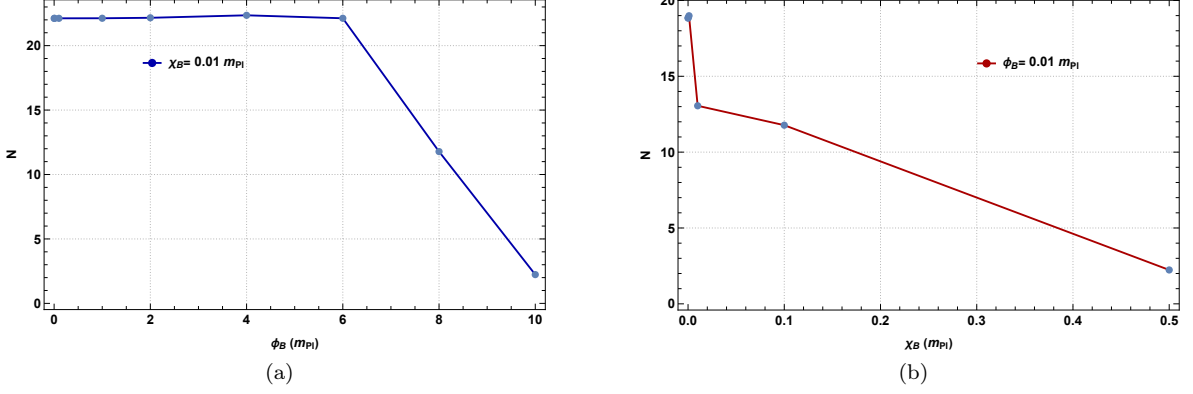


Figure 12. (a) Variation of the number of e-folds N_{inf} with respect to the initial value ϕ_B for a fixed $\chi_B = 0.01 m_{\text{Pl}}$. (b) Variation of the number of e-folds N_{inf} with respect to the initial value χ_B for fixed value of $\phi_B = 0.01 m_{\text{Pl}}$. The panels correspond to $\dot{\phi}_B < 0$ and $\dot{\chi}_B < 0$, i.e., both field velocities are negative at the bounce.

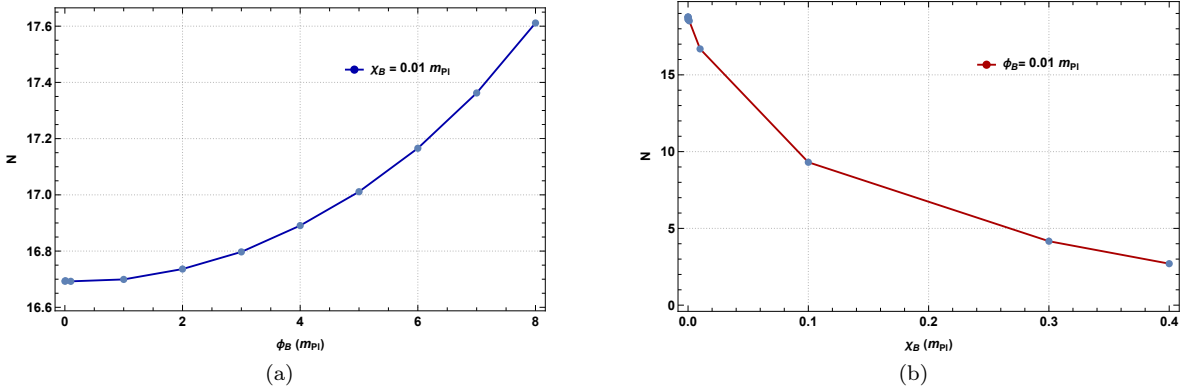


Figure 13. (a) Variation of the number of e-folds N_{inf} with respect to the initial value ϕ_B for a fixed $\chi_B = 0.01 m_{\text{Pl}}$. (b) Variation of the number of e-folds N_{inf} with respect to the initial value χ_B for fixed value of $\phi_B = 0.01 m_{\text{Pl}}$. The panels correspond to $\dot{\phi}_B < 0$ and $\dot{\chi}_B > 0$, i.e., both field velocities are opposite in sign at the bounce.

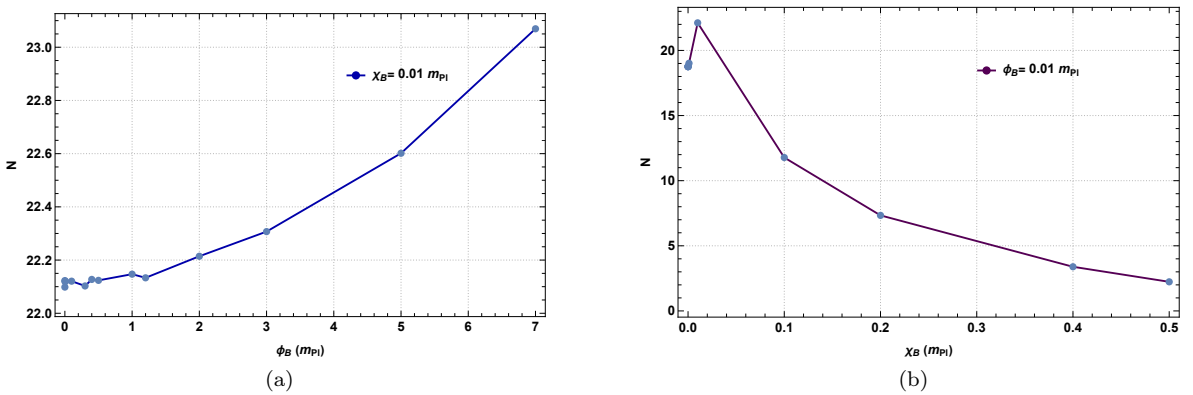


Figure 14. (a) Variation of the number of e-folds N_{inf} with respect to the initial value ϕ_B for a fixed $\chi_B = 0.01 m_{\text{Pl}}$. (b) Variation of the number of e-folds N_{inf} with respect to the initial value χ_B for fixed value of $\phi_B = 0.01 m_{\text{Pl}}$. The panels correspond to $\dot{\phi}_B > 0$ and $\dot{\chi}_B < 0$, i.e., both field velocities are opposite in sign at the bounce.

$\chi_B (m_{\text{Pl}})$	$t_{\text{start}} (m_{\text{Pl}}^{-1})$	$t_{\text{end}} (m_{\text{Pl}}^{-1})$	$\ln(a_i)$	$\ln(a_f)$	N_{inf}
10^{-5}	0.50	28.9	0.386215	19.2225	18.8363
10^{-4}	0.50	29.0	0.386209	19.2365	18.8503
10^{-3}	0.50	29.3	0.386217	19.3758	18.9896
10^{-2}	0.48	33.65	0.369811	13.4252	13.0554
10^{-1}	0.48	19.19	0.369768	12.1459	11.7761
0.5	0.64	5.39	0.478037	2.711	2.2330

Table V. Number of e-folds N_{inf} for varying initial values of χ_B with $\dot{\phi}_B < 0$ and $\dot{\chi}_B < 0$. The inflaton bounce value is fixed at $\phi_B = 0.01 m_{\text{Pl}}$ and $\dot{\phi}_B$ is then computed using energy density constraint. All the other initial values and model parameters are kept same as in Table II

$\phi_B (m_{\text{Pl}})$	$t_{\text{start}} (m_{\text{Pl}}^{-1})$	$t_{\text{end}} (m_{\text{Pl}}^{-1})$	$\ln(a_i)$	$\ln(a_f)$	N_{inf}
0.001	0.476	26.07	0.366498	17.0593	16.6928
0.01	0.474	26.07	0.364845	17.0593	16.6945
0.1	0.476	26.07	0.366504	17.0589	16.6924
1	0.476	26.08	0.366504	17.0657	16.6992
2	0.474	26.13	0.364863	17.1010	16.7361
3	0.474	26.21	0.364873	17.1620	16.7971
4	0.473	26.34	0.364061	17.2548	16.8907
5	0.471	26.50	0.362414	17.3736	17.0112
6	0.470	26.72	0.361602	17.5273	17.1657
7	0.470	27.03	0.361629	17.7240	17.3624
8	0.467	27.46	0.359140	17.9704	17.6113

Table VI. Number of e-folds N_{inf} for varying initial values of ϕ_B with $\dot{\phi}_B < 0$ and $\dot{\chi}_B > 0$. The bounce value of the auxiliary field is fixed to $\chi_B = 0.01 m_{\text{Pl}}$, while the clock field satisfies $\Phi_B = 0.5 m_{\text{Pl}}$ with $\dot{\chi}_B = 0.05 m_{\text{Pl}}^2$ and $\dot{\Phi}_B = 0.5 m_{\text{Pl}}^2$. The potential is computed with $m_{\text{Pl}} = 1$, $\rho_c = 0.41 m_{\text{Pl}}^4$, $m = 0.01 m_{\text{Pl}}$, $g = 10^{-5}$, $M = 1$, $\lambda = 0.3$, and $\beta = 0$. The field-space metric is trivial, $G_{IJ} = \delta_{IJ}$.

$\chi_B (m_{\text{Pl}})$	$t_{\text{start}} (m_{\text{Pl}}^{-1})$	$t_{\text{end}} (m_{\text{Pl}}^{-1})$	$\ln(a_i)$	$\ln(a_f)$	N_{inf}
10^{-8}	0.47	28.96	0.361549	19.1248	18.7633
10^{-7}	0.48	28.96	0.361542	19.1247	18.7632
10^{-6}	0.47	28.96	0.361549	19.1246	18.7631
10^{-5}	0.47	28.95	0.361549	18.9742	18.6127
10^{-4}	0.47	28.92	0.361542	18.9661	18.6046
10^{-3}	0.47	28.62	0.361550	18.8805	18.5190
10^{-2}	0.48	26.07	0.369797	17.0593	16.6895
10^{-1}	0.51	15.76	0.371296	9.67833	9.30703
0.3	0.56	8.37	0.408966	4.57327	4.16430
0.4	0.71	6.24	0.457554	3.15947	2.70192

Table VII. Number of e-folds N_{inf} for varying initial values of χ_B with $\dot{\phi}_B < 0$ and $\dot{\chi}_B > 0$. The inflaton bounce value is fixed at $\phi_B = 0.01 m_{\text{Pl}}$, while the clock field satisfies $\Phi_B = 0.5 m_{\text{Pl}}$ with $\dot{\chi}_B = 0.05 m_{\text{Pl}}^2$ and $\dot{\Phi}_B = 0.5 m_{\text{Pl}}^2$. The potential is computed with $m_{\text{Pl}} = 1$, $\rho_c = 0.41 m_{\text{Pl}}^4$, $m = 0.01 m_{\text{Pl}}$, $g = 10^{-5}$, $M = 1$, $\lambda = 0.3$, and $\beta = 0$. The field-space metric is trivial, $G_{IJ} = \delta_{IJ}$.

ϕ_B (m_{Pl})	t_{start} (m_{Pl}^{-1})	t_{end} (m_{Pl}^{-1})	$\ln(a_i)$	$\ln(a_f)$	N_{inf}
10^{-5}	0.50	33.65	0.386216	22.4846	22.09838
10^{-4}	0.474	33.66	0.364865	22.4877	22.12283
10^{-3}	0.474	33.65	0.364858	22.4846	22.11974
10^{-2}	0.474	33.65	0.364858	22.4847	22.11984
10^{-1}	0.474	33.65	0.364865	22.4855	22.12064
0.3	0.480	33.60	0.369824	22.4725	22.10268
0.4	0.470	33.65	0.361554	22.4888	22.12725
0.5	0.480	33.66	0.369827	22.4935	22.12367
1	0.476	33.69	0.366522	22.5135	22.14698
1.2	0.50	33.69	0.386234	22.5195	22.13327
2	0.47	33.77	0.361574	22.5759	22.21433
3	0.47	33.88	0.361588	22.6686	22.30701
5	0.47	34.25	0.361620	22.9631	22.60148
7	0.465	34.91	0.357502	23.4269	23.06940

Table VIII. Number of e-folds N_{inf} for varying values of ϕ_B with $\dot{\phi}_B > 0$ and $\dot{\chi}_B < 0$. The auxiliary field is fixed at $\chi_B = 0.01 m_{\text{Pl}}$ and the clock field at $\Phi_B = 0.5 m_{\text{Pl}}$ with $\dot{\chi}_B = -0.05 m_{\text{Pl}}^2$ and $\dot{\Phi}_B = 0.5 m_{\text{Pl}}^2$. The potential uses $m_{\text{Pl}} = 1$, $\rho_c = 0.41 m_{\text{Pl}}^4$, $m = 0.01 m_{\text{Pl}}$, $g = 10^{-5}$, $M = 1$, $\lambda = 0.3$, and $\beta = 0$, with a trivial field-space metric $G_{IJ} = \delta_{IJ}$.

χ_B (m_{Pl})	t_{start} (m_{Pl}^{-1})	t_{end} (m_{Pl}^{-1})	$\ln(a_i)$	$\ln(a_f)$	N_{inf}
10^{-8}	0.476	28.94	0.366512	19.1189	18.7524
10^{-7}	0.476	28.94	0.366505	19.1188	18.7523
10^{-6}	0.474	28.95	0.364859	19.1220	18.7571
10^{-5}	0.474	28.96	0.364859	19.1263	18.7614
10^{-4}	0.474	28.99	0.364853	19.1484	18.7835
10^{-3}	0.474	29.31	0.364861	19.3789	19.0140
10^{-2}	0.476	33.65	0.366511	22.4847	22.1182
10^{-1}	0.479	19.19	0.368946	12.1460	11.7771
0.2	0.494	12.95	0.380853	7.71560	7.3347
0.4	0.567	7.19	0.431005	3.82079	3.3898
0.5	0.638	5.39	0.476691	2.71101	2.2343

Table IX. Number of e-folds N_{inf} for varying initial values of χ_B with $\dot{\phi}_B > 0$ and $\dot{\chi}_B < 0$. The inflaton bounce value is fixed at $\phi_B = 0.01 m_{\text{Pl}}$, while the clock field satisfies $\Phi_B = 0.5 m_{\text{Pl}}$ with $\dot{\chi}_B = -0.05 m_{\text{Pl}}^2$ and $\dot{\Phi}_B = 0.5 m_{\text{Pl}}^2$. The potential is computed with $m_{\text{Pl}} = 1$, $\rho_c = 0.41 m_{\text{Pl}}^4$, $m = 0.01 m_{\text{Pl}}$, $g = 10^{-5}$, $M = 1$, $\lambda = 0.3$, and $\beta = 0$. The field-space metric is trivial, $G_{IJ} = \delta_{IJ}$.

the literature [33, 72, 83–86] as follows:

$$\begin{aligned}
x_\phi &\equiv \frac{\dot{\phi}}{\sqrt{2\rho_c}}, & x_\chi &\equiv \frac{\dot{\chi}}{\sqrt{2\rho_c}}, & x_\Phi &\equiv \frac{\dot{\Phi}}{\sqrt{2\rho_c}}, \\
y_\phi &\equiv \frac{m\phi}{\sqrt{2\rho_c}}, & y_\chi &\equiv \frac{\chi}{M}, & y_\Phi &\equiv \frac{\Phi}{M}
\end{aligned} \quad (4.3)$$

Additionally, we define a parameter $z \equiv \frac{\rho}{\rho_c}$. Substituting the dimensionless variables into the energy density equation and normalizing it with critical density yields a constraint that must be satisfied by all physical trajectories in the phase space,

$$z = x_\phi^2 + x_\chi^2 + x_\Phi^2 + y_\phi^2 + \frac{g^2 M^2}{m^2} y_\phi^2 y_\chi^2 + \frac{\lambda M^4}{4\rho_c} (y_\chi^2 - 1)^2. \quad (4.4)$$

The modified Friedmann equation (2.15a) then becomes,

$$H^2 = \frac{\kappa\rho_c}{3} z(1-z). \quad (4.5)$$

In LQC, the modified Friedmann equation imposes a fundamental upper bound on the energy density,

$$0 \leq z \equiv \frac{\rho}{\rho_c} \leq 1. \quad (4.6)$$

Consequently, the dynamical variables cannot take arbitrary values, since they must satisfy the energy–density constraint (4.4). The physically admissible phase space is therefore not the entire dynamical space, but a bounded submanifold defined by the condition 4.6. In order to analyze the global structure of the phase space and correctly identify the allowed locus of fixed points, it is convenient to compactify this bounded variable.

To achieve this, we introduce a trigonometric parametrization[87],

$$z = \sin^2 \theta, \quad 0 \leq \theta \leq \pi, \quad (4.7)$$

which automatically enforces the physical bound on the energy density. In terms of this variable, the modified

$(\dot{\phi}_B, \dot{\chi}_B)$	$\phi_B (m_{\text{Pl}})$	$\chi_B (m_{\text{Pl}})$	$t_{\text{start}} (m_{\text{Pl}}^{-1})$	$t_{\text{end}} (m_{\text{Pl}}^{-1})$	$\ln(a_i)$	$\ln(a_f)$	N_{inf}
(+, +)	1	0.01	0.66	51.9	0.404	13.516	13.111
	2	0.01	0.46	88.6	0.252	33.606	33.354
	3	0.01	0.34	122.5	0.137	59.556	59.419
	3.1	0.01	0.33	125.7	0.127	62.294	62.166
	3.2	0.01	0.32	128.9	0.117	65.037	64.920
	3.3	0.01	0.31	132.1	0.107	67.780	67.673
(-, -)	3	0.001	0.33	101.3	0.230	42.683	42.452
	3.2	0.0001	0.31	108.93	0.207	48.495	48.287
	3.2	10^{-5}	0.31	108.9	0.207	48.493	48.285
	3.3	10^{-5}	0.29	112.6	0.186	51.456	51.269
	3.4	10^{-5}	0.28	116.3	0.174	54.449	54.274
	3.6	10^{-6}	0.26	123.5	0.151	60.529	60.377
(+, -)	2	0.1	0.55	88.8	0.329	33.694	33.364
	3	0.1	0.41	121.7	0.208	58.846	58.638
	3	0.01	0.35	122.5	0.148	59.556	59.407
	3.2	0.01	0.33	128.9	0.128	65.019	64.890
	3.1	0.001	0.34	125.7	0.137	62.295	62.157
	3.05	0.0001	0.34	124.1	0.138	60.927	60.789
(-, +)	3	0.1	0.24	101.61	0.134	42.888	42.754
	3.3	0.01	0.24	112.6	0.140	51.441	51.300
	3.5	0.001	0.27	120	0.162	57.467	57.305
	3.5	0.0001	0.3	120	0.189	57.470	57.280
	3.6	0.0001	0.26	123.5	0.145	60.421	60.275
	3.7	10^{-5}	0.3	127	0.177	63.465	63.288

Table X. Number of inflationary e-folds N_{inf} obtained from the numerical analysis for different velocity sign configurations at the bounce in the KED scenario with $\phi_B > \phi_c$, $\phi_c = 0.0062$, using Eq. (3.7). The analysis is presented for all four velocity sign configurations. The parameter values used are $m = 1.50 \times 10^{-1} m_{\text{Pl}}$, $g = 8 \times 10^{-1}$, $M = 4.97 \times 10^{-3} m_{\text{Pl}}$, and $\lambda = 1$ [82]. The initial condition for the clock field is chosen as $\Phi_B = 0.5 m_{\text{Pl}}$ and $\dot{\Phi}_B = 0.01 m_{\text{Pl}}^2$ in all cases. $\dot{\chi}_B = -0.5 m_{\text{Pl}}^2$ when $\dot{\chi}_B < 0$ and $\dot{\chi}_B = 0.5 m_{\text{Pl}}^2$ when $\dot{\chi}_B > 0$. Here, i refers to "initial" and f refers to "final" in correspondence with onset and end of slow-roll.

Friedmann equation gives

$$H = \pm \sqrt{\frac{\kappa \rho_c}{12}} \sin(2\theta). \quad (4.8)$$

Equation (4.8) shows that the Hubble parameter naturally splits into two branches:

- the positive branch $H > 0$, corresponding to the expanding universe,
- the negative branch $H < 0$, corresponding to the contracting universe.

The bounce occurs at $z = 1$, or equivalently $\theta = \frac{\pi}{2}$, where $H = 0$. Similarly, $z = 0$ corresponds to $\dot{\theta} = 0$ or $\theta = \pi$, representing the classical low-density regime. Thus, the trigonometric compactification provides a global parametrization of the physical phase space, smoothly connecting the contracting and expanding branches through the bounce.

In terms of the dynamical variables, the energy-density constraint now takes the compact form

$$\sin^2 \theta = x_\phi^2 + x_\chi^2 + x_\Phi^2 + y_\phi^2 + \frac{g^2 M^2}{m^2} y_\phi^2 y_\chi^2 + \frac{\lambda M^4}{4\rho_c} (y_\chi^2 - 1)^2. \quad (4.9)$$

This representation makes the bounded nature of the physical phase space explicit and ensures that the autonomous system evolves on a compact submanifold. Fixed points must therefore satisfy not only the vanishing of the dynamical derivatives, but also the compactified constraints (4.8),(4.9).

We introduce the dimensionless time variable $\tau = Mt$ so that the time derivative transforms as $\frac{d}{d\tau} = \frac{1}{M} \frac{d}{dt}$. Using this relation and the definitions in Eq. (4.3), the autonomous system becomes:

$$\frac{dx_\phi}{d\tau} = -\frac{3H}{M} x_\phi - \frac{m}{M} y_\phi - \frac{g^2 M}{m} y_\phi y_\chi^2, \quad (4.10)$$

$$\frac{dx_\chi}{d\tau} = -\frac{3H}{M}x_\chi - \frac{g^2\sqrt{2\rho_c}}{m^2}y_\phi^2y_\chi - \frac{\lambda M^2}{\sqrt{2\rho_c}}y_\chi(y_\chi^2 - 1), \quad (4.11)$$

$$\frac{dx_\Phi}{d\tau} = -\frac{3H}{M}x_\Phi, \quad (4.12)$$

$$\frac{dy_\phi}{d\tau} = \frac{m}{M}x_\phi, \quad (4.13)$$

$$\frac{dy_\chi}{d\tau} = \frac{\sqrt{2\rho_c}}{M^2}x_\chi, \quad (4.14)$$

$$\frac{dy_\Phi}{d\tau} = \frac{\sqrt{2\rho_c}}{M^2}x_\Phi. \quad (4.15)$$

To study the stability of this model, we linearize the system by expanding the evolution equations around the fixed points and retaining terms up to first order in perturbations. This leads to a system of linear differential equations whose coefficients are encapsulated in the Jacobian matrix given by $\mathcal{J}_{ij} \equiv \frac{\partial F_i}{\partial X_j}$ where $F_i \in \left\{ \frac{dx_\phi}{d\tau}, \frac{dx_\chi}{d\tau}, \frac{dx_\Phi}{d\tau}, \frac{dy_\phi}{d\tau}, \frac{dy_\chi}{d\tau}, \frac{dy_\Phi}{d\tau} \right\}$ and $X_j \in \{x_\phi, x_\chi, x_\Phi, y_\phi, y_\chi, y_\Phi\}$. The fixed points of the system are obtained by requiring the simultaneous vanishing of all autonomous derivatives,

$$\frac{dx_\phi}{d\tau} = \frac{dx_\chi}{d\tau} = \frac{dx_\Phi}{d\tau} = \frac{dy_\phi}{d\tau} = \frac{dy_\chi}{d\tau} = \frac{dy_\Phi}{d\tau} = 0. \quad (4.16)$$

and then solving the resulting algebraic equations subject to the constraints (4.5) and (4.4) are presented in the table below. These points correspond to the asymptotic cosmological states of the model, and their stability analysis follows from a linearization of this autonomous system around each critical point.

The dynamical system analysis reproduces the structure given by true vacuum and false vacuum discussed in Subsec. III A, at the level of phase-space fixed points. The fixed point P_2 corresponds to the configuration $(\phi, \chi) = (0, 0)$, where all kinetic terms vanish and the energy density is entirely dominated by the constant potential. This configuration therefore represents the false vacuum state.

The stability analysis shows that P_2 is a saddle point: in the expanding branch, some directions are unstable, while in the contracting branch the signs of the real parts of the eigenvalues are reversed. This behavior reflects the time-reversal symmetry of the Hubble friction term, which changes sign between the expanding and contracting phases. The equation of state at this point is $\omega = \frac{P}{\rho} = -1$, which corresponds to a vacuum-dominated or inflationary state.

In contrast, the fixed points P_1 and P_3 correspond to the configurations

$$(\phi, \chi) = (0, -M), \quad (\phi, \chi) = (0, +M), \quad (4.17)$$

which are precisely the true vacuum states of the theory. At these points, all kinetic energies vanish, the

potential energy is zero, and the total energy density satisfies $\rho = 0$. Consequently, the Hubble parameter also vanishes, and the universe approaches a static, zero-energy configuration. These points therefore represent the late-time vacuum states reached after the waterfall transition.

The eigenvalues at P_1 and P_3 are purely imaginary, with additional zero eigenvalues, and are identical in both the expanding and contracting branches. These fixed points thus form non-hyperbolic centers corresponding to a continuous surface of equilibria parameterized by the χ and clock-field directions. As discussed in standard dynamical systems literature [88], when fixed points form a continuous set rather than isolated points, linear stability analysis becomes inconclusive along the neutral directions. In such cases, the dynamics is governed by the center manifold, and higher-order or numerical analysis is required to determine the ultimate stability properties of the system. Physically, this degeneracy arises because the clock field is free and does not contribute to the potential energy, leading to a conserved direction in phase space.

From a global phase-space perspective, the cosmological evolution in this model can therefore be understood as a transition from the false vacuum fixed point P_2 to one of the true vacuum fixed points P_1 or P_3 . Inflation proceeds while the system remains close to the false vacuum configuration. Once the critical value ϕ_c is reached, the χ direction becomes unstable, triggering the waterfall transition. The trajectory then rapidly evolves toward one of the symmetry-broken minima, where it settles into the corresponding vacuum fixed point. This dynamical systems picture therefore reproduces the standard hybrid inflation scenario.

V. BACKGROUND DYNAMICS FOR THE STRING-INSPIRED MODEL

A. Numerical analysis

The resulting background dynamics for the model studied here are presented in the following panels. The universe evolves from bounce at $a = 1$, $\dot{a} = 0$ and enters into exponential expansion Fig. 15. The superinflation occurs shortly after the bounce and ends at the epoch $t = 0.180 m_{Pl}^{-1}$, $t = 0.178 m_{Pl}^{-1}$, $t = 0.178 m_{Pl}^{-1}$ for $\phi_B = 1m_{Pl}$, $\phi_B = 2m_{Pl}$, $\phi_B = 3m_{Pl}$, respectively, see Table XII. This epoch is consistently identified across multiple observables: the time derivative of the hubble parameter \dot{H} Fig. 15b, which shows the transition from positive to negative values; the acceleration \ddot{a} Fig. 16a.

Following this, the evolution proceeds through a sequence of dynamical epochs that can be identified consistently across multiple diagnostics. These distinct epochs are summarized in Table XII.

Point	Fixed point coordinates	Eigenvalues	Linear stability
Expanding branch ($H > 0$)			
$P_1^{(+)}$	$(x_\phi, x_\chi, x_\Phi, y_\phi, y_\chi, y_\Phi)$ $= (0, 0, 0, 0, -1, \bar{y}_\Phi)$	$\{\pm 0.7746i, \pm 0.01i, 0, 0\}$	Non-hyperbolic center
$P_2^{(+)}$	$(x_\phi, x_\chi, x_\Phi, y_\phi, y_\chi, y_\Phi)$ $= (0, 0, 0, 0, 0, \bar{y}_\Phi)$	$\{-2.2810, -2.1495, -2.1495, 0.1315, -4.65 \times 10^{-5}, 0\}$	Unstable saddle
$P_3^{(+)}$	$(x_\phi, x_\chi, x_\Phi, y_\phi, y_\chi, y_\Phi)$ $= (0, 0, 0, 0, 1, \bar{y}_\Phi)$	$\{\pm 0.7746i, \pm 0.01i, 0, 0\}$	Non-hyperbolic center
Contracting branch ($H < 0$)			
$P_1^{(-)}$	$(x_\phi, x_\chi, x_\Phi, y_\phi, y_\chi, y_\Phi)$ $= (0, 0, 0, 0, -1, \bar{y}_\Phi)$	$\{\pm 0.7746i, \pm 0.01i, 0, 0\}$	Non-hyperbolic center
$P_2^{(-)}$	$(x_\phi, x_\chi, x_\Phi, y_\phi, y_\chi, y_\Phi)$ $= (0, 0, 0, 0, 0, \bar{y}_\Phi)$	$\{2.2810, 2.1495, 2.1495, -0.1315, 4.65 \times 10^{-5}, 0\}$	Unstable saddle (time-reversed directions)
$P_3^{(-)}$	$(x_\phi, x_\chi, x_\Phi, y_\phi, y_\chi, y_\Phi)$ $= (0, 0, 0, 0, 1, \bar{y}_\Phi)$	$\{\pm 0.7746i, \pm 0.01i, 0, 0\}$	Non-hyperbolic center

Table XI. Critical points for the hybrid inflation model in LQC dynamical system. An overbar denotes an arbitrary constant value along that direction, indicating a continuous locus of equilibrium points rather than an isolated critical point. Such non-isolated equilibria are non-hyperbolic and their stability cannot be fully determined from linear analysis alone, requiring center manifold or higher-order analysis [88]

Epoch	Condition	$\phi_B = 1 \ m_{\text{Pl}}$	$\phi_B = 2 \ m_{\text{Pl}}$	$\phi_B = 3 \ m_{\text{Pl}}$
End of superinflation	$\rho = 0.205 \ m_{\text{Pl}}^4$	0.180	0.178	0.178
KE=PE	$\omega = 0$	48.4	33.9	26.0
Onset of slow-roll	$\omega = -1/3$	60.9	42.9	33.3
End of slow-roll	$\omega = -1/3$	8644	6558	5050
$\log a_{\text{initial}}$	—	1.921	1.840	1.775
$\log a_{\text{final}}$	—	64.10	57.36	50.62
e-folds (N_{inf})	$\log a_f - \log a_i$	62.18	55.52	48.85

Table XII. Characteristic epochs of the quantum corrected background evolution for the string-inspired model 2 with hyperbolic field space geometry, determined from the corresponding condition. The listed epochs are in Planck units (m_{Pl}^{-1}).

In particular, the ϕ field initially increases from the bounce and then settles to a nearly constant value, while the χ field displays a sharper evolution, it increases briefly, followed by a rapid decline and eventual decay, see Figs. 17, 18. This contrasting behavior highlights the asymmetric role of the component fields in driving the dynamics, with ϕ providing a long-lived background while χ rapidly decays, leaving the system effectively dominated by the ϕ field eventually.

When superinflation ends, the energy density ρ Fig. 19, reaches half of the critical value, $\rho = 0.205 \ m_{\text{Pl}}^4$, at the same epoch in consistence with previous indicators.

As expected, the total energy density gradually decreases as the universe evolves. Initially, the kinetic energy dominates the total energy density, driving the dynamics near the bounce. As the evolution progresses, the potential energy rises, eventually overtaking the kinetic contribution and sustaining the slow-roll phase before gradually decaying in tandem with the total energy density.

For larger initial field values, the damping of the potential energy occurs more rapidly, leading to an overall

faster approach towards the slow-roll regime. Both the kinetic and potential energy contributions show a gradual decline with time before stabilizing at late epochs, as seen in fig. 19.

Upon transition, the universe enters into the damping phase as evident from the equation-of-state parameter shown in Fig. 20a, where ω evolves slowly from 1 towards -1 . The transition epochs for distinct initial values are listed in Table XII. This behavior is consistent with the evolution of the r parameter, see Fig. 20b, which approaches values close to zero around the same epoch. Moreover, these results remain robust under variations of the initial conditions, demonstrating the stability of the background dynamics.

Once the slow-roll parameters decrease from their initially large values of $\epsilon_H, \eta_H \gg 1$ (see for example fig. 21), characteristic of the superinflationary phase, they subsequently exhibit damped oscillations about the origin, signaling the transition and gradual stabilization into the slow-roll regime.

The slow-roll phase is characterized by a sustained dominance of potential energy ($V \gg \dot{\sigma}^2/2$), nearly constant H , and $\omega \approx -1$, as seen in the corresponding plots. Both slow-roll parameters (ϵ_H, η_H) $\ll 1$, confirming ad-

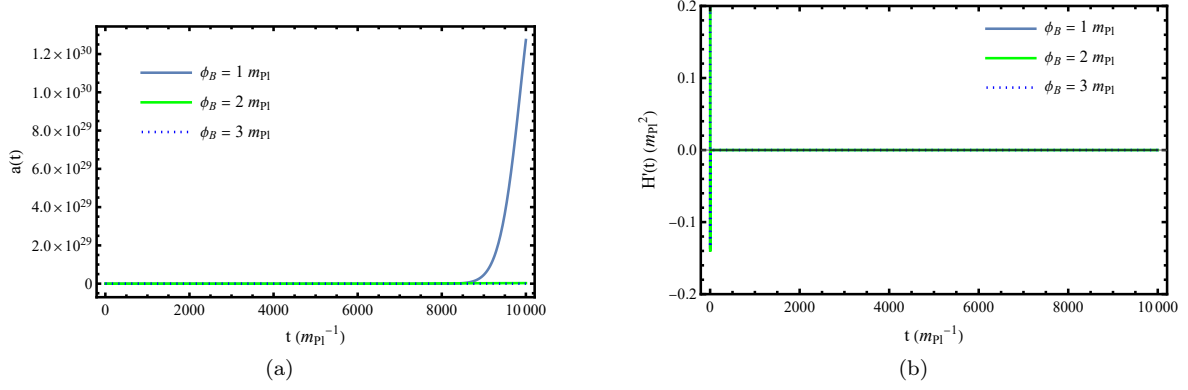


Figure 15. Evolution of (a) the scale factor $a(t)$, and (d) $H(t)$ for the string-inspired model 2 with a non-canonical hyperbolic kinetic space represented by the metric (3.10), in the LQC framework. The initial values of the field ϕ are taken as 1, 2, and 3 m_{Pl} , the model parameters are $m = 10^{-6} m_{Pl}$, $g = 3 \times 10^{-4}$, $\beta = -0.1 m_{Pl}^{-1}$ which are consistently used throughout this analysis. The χ_B value is fixed at $4.5 m_{Pl}$ and its velocity at $\dot{\chi}_B = 0.1 m_{Pl}^2$. The initial values of clock field and its velocity are fixed at $(\Phi_B, \dot{\Phi}_B) = (0.5 m_{Pl}, 0.5 m_{Pl}^2)$. These plots highlight the modifications in dynamics due to quantum corrections.

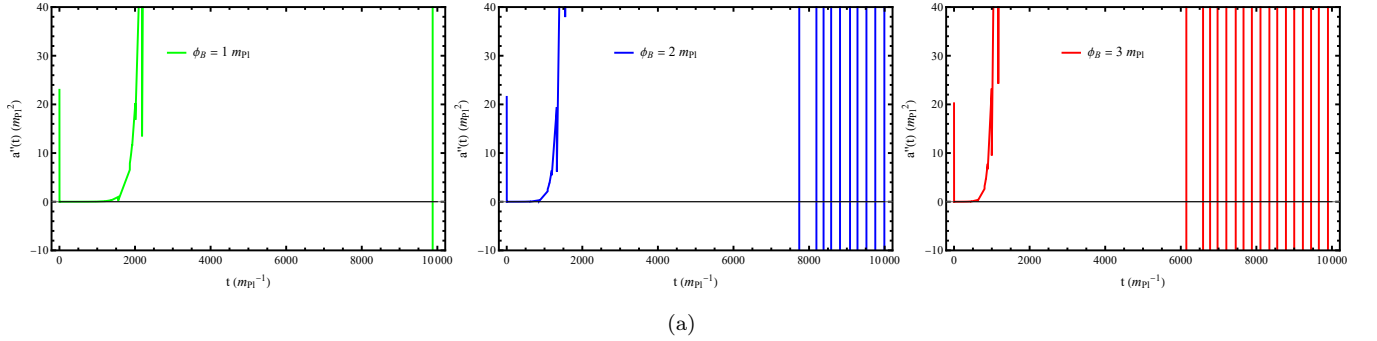


Figure 16. Each panel corresponds to the plot of $\ddot{a}(t)$ for different values of ϕ_B in the string-inspired model 2 within the LQC framework, with model parameters and initial conditions identical to those in Fig. 15. It can be clearly seen that the acceleration $\ddot{a}(t)$ remains positive throughout the slow-roll phase.

herence to slow-roll conditions throughout this period, see Fig. 21.

At later epochs, negative values of the pressure are observed in Fig. 22a, providing clear evidence for the onset and the end of the slow-roll regime and confirming that slow-roll inflation calculated with the help of Fig. 22b as per the definition in Eq. (2.19), is achieved for several number of e-folds in this model. The total number of e-folds for each ϕ_B value are summarized in Table XII.

The decrease in N_{inf} with increasing ϕ_B reflects that larger initial field amplitudes correspond to a steeper effective potential slope, causing faster field evolution and earlier exit from slow-roll. Conversely, smaller ϕ_B values yield a gentler potential gradient, producing longer inflationary durations.

To understand how the pre-inflationary conditions influence the total expansion, we evaluated N_{inf} as a func-

tion of the initial inflaton amplitude ϕ_B for several representative values of the secondary field χ_B . Similarly, we repeated the exercise by adopting the same initial amplitudes for χ_B and evaluated N_{inf} as a function of the initial values of the inflaton field. The results are presented in Fig. 23a, where each curve corresponds to a distinct χ_B value, illustrating the interplay between the two-field dynamics.

For a more detailed examination, comprehensive numerical values corresponding to specific cases are tabulated in Tables XIII and XIV. It should be noted that these plots and tables correspond to configurations with positive initial field velocities, i.e., $\dot{\phi}_B > 0$ and $\dot{\chi}_B > 0$.

In Table XIII, the number of e-folds decreases monotonically with increasing ϕ_B . For extremely small inflaton amplitudes ($\phi_B \lesssim 10^{-2} m_{Pl}$), the total e-folding saturates around $N_{inf} \approx 33$. As the inflaton amplitude increases, the total number of e-folds drops gradually.

A contrasting behaviour is observed in Table XIV. In this case, the number of e-folds grows sharply with increasing χ_B . At $\chi_B = 4.98 m_{Pl}$, the total expansion

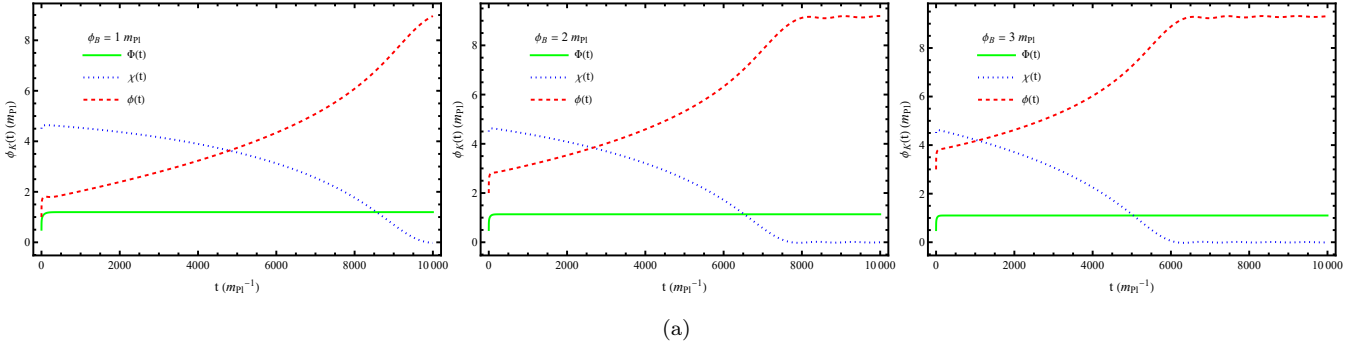


Figure 17. Evolution of the component fields $\phi(t)$, $\chi(t)$, and $\Phi(t)$ for the string-inspired model 2 in the LQC framework. Each panel, corresponding to a distinct value of ϕ_B , illustrating the dynamics of the fields from bounce onwards. The component fields evolve in opposite directions—one field grows to stabilize and eventually dominate the dynamics, while the other decays as the universe expands. The clock field $\Phi(t)$ remains constant throughout the evolution, unaffected by the dynamical interactions.

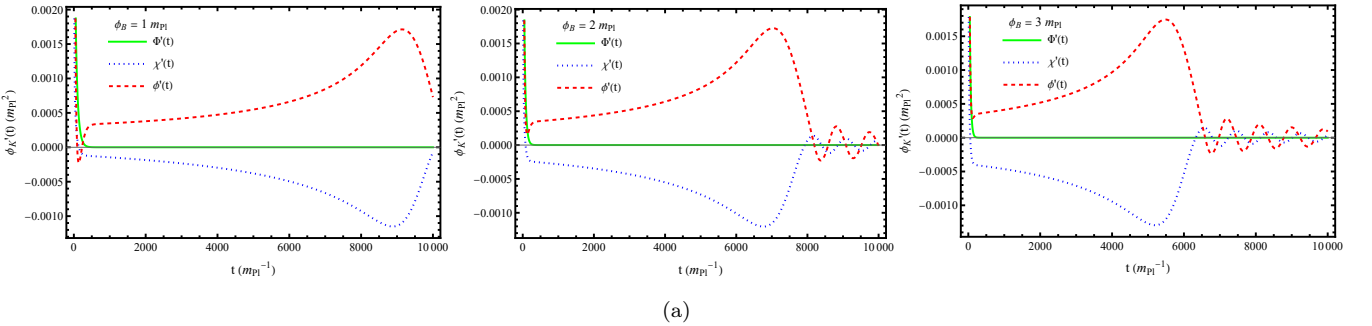


Figure 18. Each panel, corresponding to a distinct value of ϕ_B , depicts the evolution of the field velocities $\dot{\phi}(t)$, $\dot{\chi}(t)$, and $\dot{\Phi}(t)$ for the string-inspired model 2. The component field velocities evolve in opposite directions—one diminishing while the other grows—reflecting their contrasting dynamical roles.

amounts to $N_{\text{inf}} \approx 60$. The steady increase in N_{inf} with the secondary field amplitude highlights the sensitivity of the inflationary duration to its initial configuration. A larger χ_B amplifies the interaction term $\frac{1}{2}g^2\phi^2\chi^2$, effectively flattening the potential and extending the period over which the potential energy dominates over the kinetic energy. Consequently, the slow-roll conditions are satisfied for a longer time, resulting in a prolonged inflation.

As can be seen in Fig. 23, the qualitative trend remains consistent across both analyses: in each case, the dependence of N_{inf} on the varying field exhibits smooth and monotonic behaviour. For distinct fixed χ_B values, the $N(\phi_B)$ curves follow similar trend, with higher fixed χ_B values leading to systematically higher N across all ϕ_B . Conversely, for distinct fixed ϕ_B values, the $N(\chi_B)$ curves display the same monotonic growth pattern, but higher fixed ϕ_B values correspond to lower N_{inf} across all χ_B . In the fixed χ_B case, N_{inf} decreases with increasing ϕ_B , whereas in the fixed ϕ_B case, N_{inf} increases with increasing χ_B . This complementary pattern shows the dual role of the two fields in controlling the total inflationary expansion.

As can be seen in Fig. 23, the qualitative trend re-

mains consistent across both analyses: in each case, the dependence of N_{inf} on the varying field exhibits smooth and monotonic behaviour. For distinct fixed χ_B values, the $N(\phi_B)$ curves follow similar shapes, with higher fixed χ_B values leading to systematically higher N_{inf} across all ϕ_B . Conversely, for distinct fixed ϕ_B values, the $N(\chi_B)$ curves display the same monotonic growth pattern, but higher fixed ϕ_B values correspond to lower N_{inf} across all χ_B . In the fixed χ_B case, N_{inf} decreases with increasing ϕ_B , whereas in the fixed ϕ_B case, N_{inf} increases with increasing χ_B . This complementary pattern shows the dual role of the two fields in controlling the total inflationary expansion.

We first discuss the case where the initial field velocities are negative, i.e., $(\dot{\phi}_B < 0, \dot{\chi}_B < 0)$. Similar to the $(\dot{\phi}_B > 0, \dot{\chi}_B > 0)$ case, this configuration was found to be particularly favorable for realizing sufficient inflation. The total number of e-folds N_{inf} reaches and exceeds the observationally required $N_{\text{inf}} \simeq 60$ for suitable ranges of initial field amplitudes, both when ϕ_B or χ_B are held fixed. The numerical results are summarized in Tables XV and XVI.

However, the variation in N_{inf} is noticeably sharper when χ_B is fixed and ϕ_B is varied, where $N_{\text{inf}} \simeq 60$ for

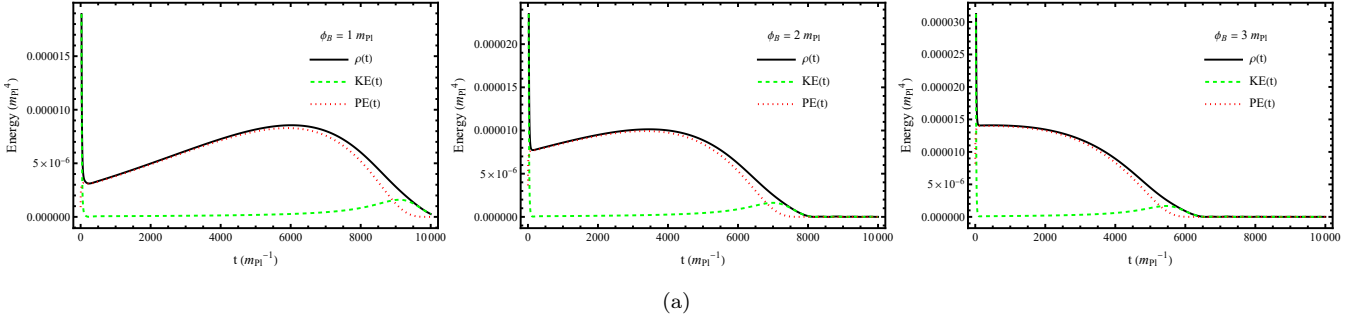


Figure 19. Comparison of the kinetic energy, potential energy, and total energy density during the evolution of the string-inspired model 2. Each panel corresponds to a distinct initial value of ϕ_B . The potential energy gradually overtakes the total energy density during the slow-roll phase as the kinetic energy rapidly declines.

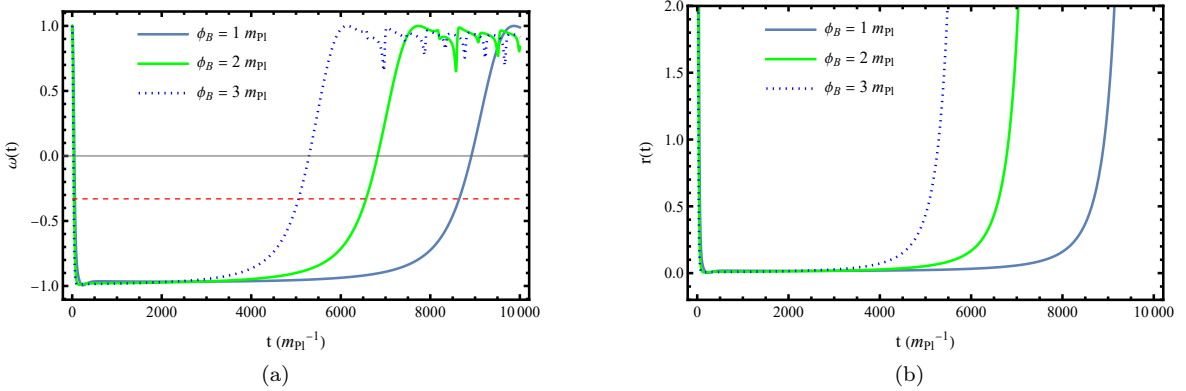


Figure 20. Evolution of (a) the equation-of-state parameter $\omega(t)$ and (b) the kinetic-to-potential energy ratio $r(t)$ for the string-inspired model 2 in the LQC framework. The red dashed line marks $\omega = -\frac{1}{3}$, indicating the threshold for the onset and termination of the slow-roll phase. A smooth transition is observed from ($\omega \approx +1$) to ($\omega \approx -1$). The slow-roll phase concludes as ω rises above $-\frac{1}{3}$. Both panels consistently demonstrate a finite, successful, and PED inflationary regime.

$\chi_B \sim 3.9 m_{\text{Pl}}$, compared to the case of fixed ϕ_B and varying χ_B , where $N_{\text{inf}} \simeq 60$ for $\chi_B \sim 5.35 m_{\text{Pl}}$. This indicates that the inflaton amplitude ϕ_B exerts a stronger control on the inflationary duration than the auxiliary field amplitude χ_B , leading to a more abrupt transition between short and long inflationary phases. Similar to the trend in the ($\dot{\phi}_B > 0, \dot{\chi}_B > 0$) case, in Fig. 24, for fixed χ_B , N_{inf} increases as ϕ_B decreases, whereas for fixed ϕ_B , N_{inf} increases with increasing χ_B . Taken together, these results demonstrate that within the hybrid model, negative initial field velocities can naturally lead to sufficiently long inflationary phases.

Tables XVII and XVIII summarize the outcomes when the initial field velocities have opposite signs (specifically $\dot{\phi}_B < 0$ and $\dot{\chi}_B > 0$). Same results can be directly observed in Fig. 25.

The total number of e-folds N_{inf} exhibits an extremely strong sensitivity to the initial amplitudes in this configuration. When χ_B is fixed at $1 m_{\text{Pl}}$ and ϕ_B is varied in Table XVIII, N_{inf} attains extraordinarily large values for very small inflaton amplitudes: for $\phi_B \lesssim 10^{-2} m_{\text{Pl}}$ one finds $N_{\text{inf}} \sim \mathcal{O}(10^4) - \mathcal{O}(10^5)$. As ϕ_B increases, N_{inf}

falls dramatically, by $\phi_B \sim \mathcal{O}(10)$ the e-fold count is of order 10^3 , and for $\phi_B \gtrsim 25 m_{\text{Pl}}$ the inflationary expansion becomes negligible ($N_{\text{inf}} \lesssim \mathcal{O}(10^1)$). Thus, in the mixed-sign case the inverse correlation between ϕ_B and N_{inf} is much steeper than in the same-sign velocity cases discussed above.

When ϕ_B is fixed at $1 m_{\text{Pl}}$ and χ_B is varied (Table XVII), N_{inf} likewise grows rapidly with increasing χ_B . Very small χ_B already produce extremely large e-fold numbers (hundreds to thousands), while larger χ_B yield enormous N_{inf} . Hence, both decreasing ϕ_B (at fixed small χ_B) and increasing χ_B (at fixed small ϕ_B) drive the system into regimes of extremely prolonged inflation in this mixed-sign-velocity configuration.

With opposite signs of the initial velocities the two fields initially move in opposite directions in field space, which can significantly slow the collective motion along the adiabatic direction. The interaction term $\frac{1}{2}g^2\phi^2\chi^2$ then sustains potential dominance for a much longer interval than in the same-sign cases, producing greatly extended slow-roll-like evolution. In other words, the initial kinetic-energy partition and the relative directions of field motion strongly affect how and when the system ap-

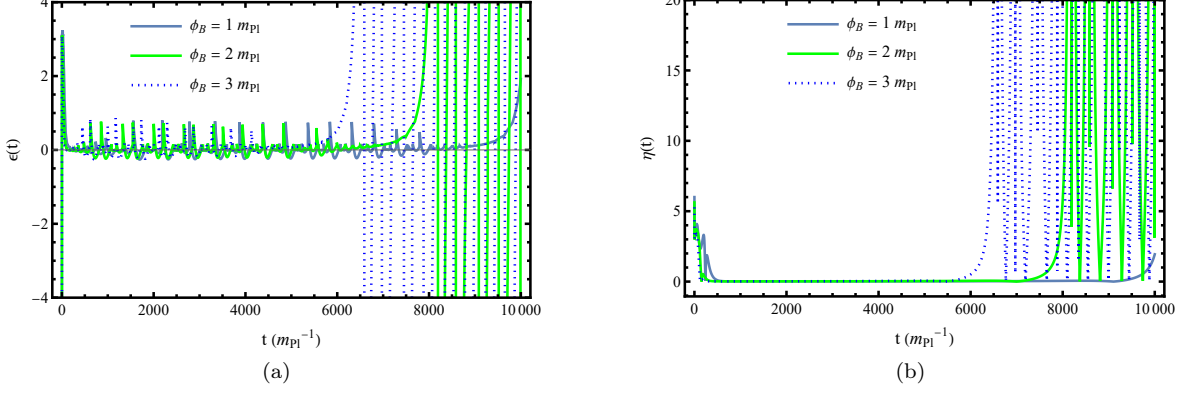


Figure 21. Evolution of the slow-roll parameters (a) $\epsilon_H(t)$ and (b) $\eta_H(t)$ for the string-inspired model 2 in the LQC framework. These plots illustrate the onset and the end of slow-roll phase. Both $\epsilon_H, \eta_H \ll 1$ during the regime, while $\epsilon_H < 0$ during superinflation.

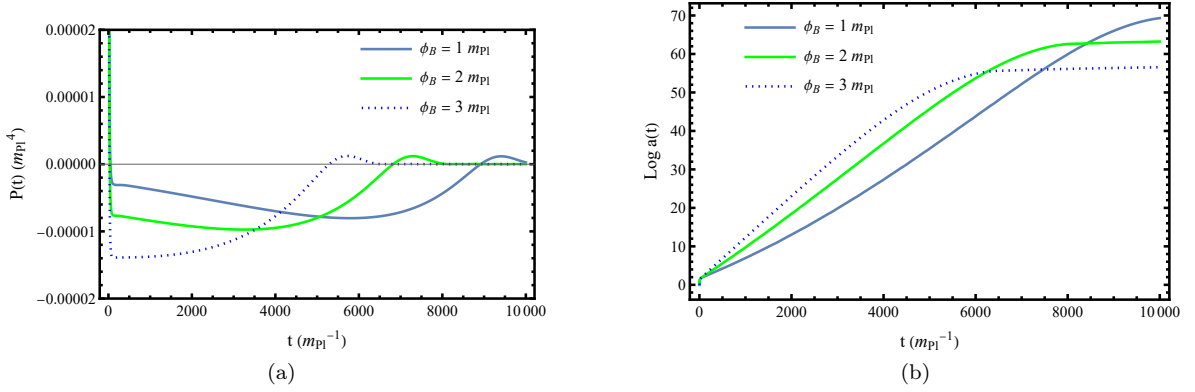


Figure 22. The above figure shows the evolution of (a) the pressure and (b) $\log a(t)$ for the string-inspired model 2 in the LQC framework. The pressure transitions to negative values as the system enters the slow-roll regime and remains negative throughout this phase, consistent with the conditions required for accelerated expansion.

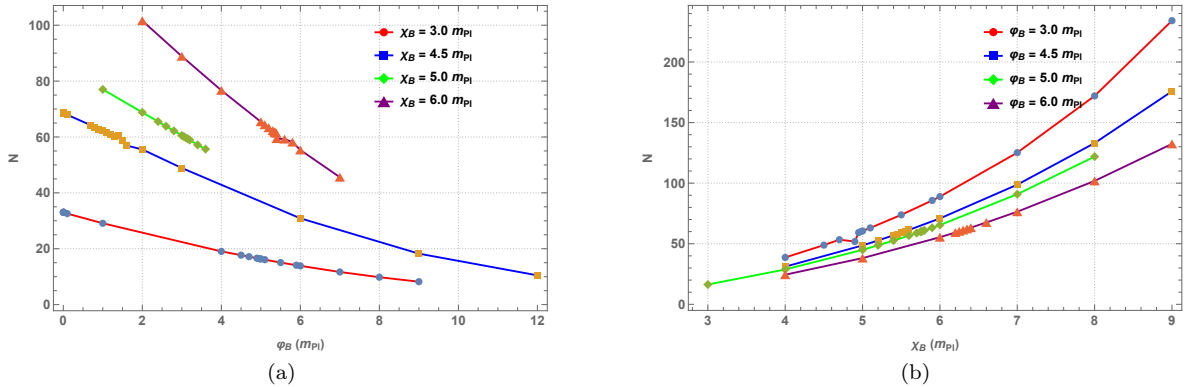


Figure 23. (a) Variation of N_{inf} with respect to the initial inflaton value ϕ_B for different values of the secondary field amplitude χ_B . Each curve corresponds to a distinct χ_B value as labeled. (b) Variation of the N_{inf} with respect to the initial values of χ_B where each curve in this panel corresponds to the distinct ϕ_B value. Both the graphs are obtained by adopting same distinct values for χ_B and ϕ_B for comparison. The panels correspond to $\dot{\phi}_B > 0$ and $\dot{\chi}_B > 0$, i.e., both field velocities are positive at the bounce.

$\phi_B (m_{\text{Pl}})$	$t_{\text{start}} (m_{\text{Pl}}^{-1})$	$t_{\text{end}} (m_{\text{Pl}}^{-1})$	$\ln(a_i)$	$\ln(a_f)$	N_{inf}
0.000001	761.1798	9602.492	3.195457	36.277163	33.081706
0.00001	761.1467	9602.357	3.195432	36.277074	33.081642
0.0001	761	9600	3.19534	36.271	33.07566
0.001	758	9578	3.193	36.22	33.027
0.005	743.2	9526	3.18143	36.212	33.03057
0.009	729.8	9475	3.17066	36.203	33.03234
0.01	727	9457	3.1684	36.17	33.016
0.1	528	8570	2.968	35.55	32.582
1.0	87	5534	2.015	31.13	29.115
4.0	39.3	2384	1.8343	20.9392	19.049
4.5	36.1	2092	1.8114	19.515	17.7036
4.7	34.9	1985	1.8018	18.963	17.1612
4.9	33.83	1882	1.79306	18.412	16.61894
4.95	33.54	1858	1.79050	18.282	16.4915
4.98	33.4	1843	1.78939	18.199	16.40961
5.0	33.39	1833	1.7898	18.1442	16.3544
5.1	32.88	1784	1.7853	17.8711	16.0858
5.5	31.03	1602.9	1.7689	16.827	15.0581
5.9	29.33	1444	1.7523	15.858	14.1057
6.0	28.87	1407	1.7473	15.624	13.8767
7.0	25.53	1078	1.7111	13.395	11.6839
8.0	22.8	829	1.6762	11.487	9.8108
9.0	20.6	638	1.6444	9.851	8.2066

Table XIII. This table shows the number of e-folds, N_{inf} , for various initial values of ϕ_B , corresponding to the string-inspired model 2, with model parameters $m = 10^{-4}m_{\text{Pl}}$, $g = 10^{-6}$, and $\beta = -0.1m_{\text{Pl}}^{-1}$, where $m_{\text{Pl}} = 1$. Field value χ_B at bounce is fixed at $3m_{\text{Pl}}$. This case corresponds to both $\dot{\phi}_B > 0$ and $\dot{\chi}_B > 0$, i.e., the initial field velocities are positive at the bounce.

$\chi_B (m_{\text{Pl}})$	$t_{\text{start}} (m_{\text{Pl}}^{-1})$	$t_{\text{end}} (m_{\text{Pl}}^{-1})$	$\ln(a_i)$	$\ln(a_f)$	N_{inf}
4.0	36.9	4372	1.8063	40.47	38.6637
4.5	33.19	5051	1.7739	50.63	48.856
4.7	31.95	5338	1.7624	55.11	53.348
4.9	30.77	5639	1.7510	53.58	51.829
4.95	30.6	5708	1.7495	61.03	59.2805
4.98	30.31	5754	1.7461	61.77	60.0239
5.0	30.4	5791	1.7475	62.30	60.5525
5.1	29.7	5940	1.7400	64.80	63.0600
5.5	27.8	6587	1.7200	75.55	73.8300
5.9	26.1	7283	1.7005	87.42	85.7195
6.0	25.6	7466	1.6939	90.58	88.8861
7.0	22.29	9565	1.6800	126.85	125.1700
8.0	19.77	12385	1.6130	173.60	171.9870
9.0	17.68	16663	1.5780	132.80	131.2220

Table XIV. This table shows the values of the number of e-folds, N_{inf} , for various initial values of χ_B . Field value ϕ_B at bounce is fixed at $3m_{\text{Pl}}$. This case corresponds to both $\dot{\phi}_B > 0$ and $\dot{\chi}_B > 0$, i.e., the initial field velocities are positive at the bounce.

$\phi_B (m_{\text{Pl}})$	$t_{\text{start}} (m_{\text{Pl}}^{-1})$	$t_{\text{end}} (m_{\text{Pl}}^{-1})$	$\ln(a_i)$	$\ln(a_f)$	N_{inf}
26.0	5.5	19.1	1.22242	2.09211	0.86969
24.0	5.7	31.5	1.22868	2.65097	1.42229
22.0	6.1	52.6	1.24891	3.44064	2.19173
20.0	6.7	89	1.22313	3.61277	2.38964
21.5	6.3	60.2	1.26099	3.69418	2.43319
21.0	6.4	68.2	1.26516	3.95464	2.68948
20.5	6.5	77.9	1.26912	4.25315	2.98403
15.0	9.0	335	1.33524	9.72349	8.38825
10.0	13.5	1278	1.50783	24.1588	22.65097
8.0	17.88	10074	1.5852	33.99	32.4048
7.5	18.31	2524	1.6052	36.91	35.3048
7.0	19.78	2892	1.6301	40.02	38.38990
4.0	36.9	6431	1.7479	61.27	59.5221
3.9	37.91	6605	1.8249	62.012	60.1871
3.8	39.08	6776	1.8335	62.712	60.8785
3.7	40.30	6956	1.8421	63.433	61.5909
3.0	51.6	8317	1.9083	68.11	66.2017
2.0	87.4	10576	2.33	73.28	70.95
1.5	265	11733	2.48845	74.9067	72.41825
1.0	520	12958	2.92866	76.215	73.28634
0.1	1628	16385	4.05654	78.6802	74.62366

Table XV. This table shows the number of e-folds, N_{inf} , for various initial values of ϕ_B . Field value χ_B at bounce is fixed at $5 m_{\text{Pl}}$. This case corresponds to both $\dot{\phi}_B < 0$ and $\dot{\chi}_B < 0$, i.e., the initial field velocities are negative at the bounce.

$\chi_B (m_{\text{Pl}})$	$t_{\text{start}} (m_{\text{Pl}}^{-1})$	$t_{\text{end}} (m_{\text{Pl}}^{-1})$	$\ln(a_i)$	$\ln(a_f)$	N_{inf}
2.0	68.5	1339	1.9982	8.58773	6.58953
3.0	47.0	2596	1.8930	19.81	17.917
4.0	35.7	3728	1.8110	34.48	32.669
5.0	28.7	4949	1.7440	53.95	52.206
5.1	28.05	5078	1.7369	56.19	54.4531
5.2	27.47	5211	1.7301	59.49	57.7599
5.3	27.01	5343	1.7252	60.84	59.1148
5.35	26.778	5410	1.72255	62.034	60.31145
5.4	26.497	5481	1.7191	63.269	61.5499
5.45	26.236	5553	1.71590	64.397	62.6811
6.0	23.89	6338	1.6869	79.00	77.3131
7.0	20.46	7988	1.6378	110.8	109.1622
8.0	17.88	10074	1.5947	150.8	149.2053

Table XVI. This table shows the number of e-folds, N_{inf} , for various initial values of χ_B . Field value ϕ_B at bounce is fixed at $5 m_{\text{Pl}}$. This case corresponds to both $\dot{\phi}_B < 0$ and $\dot{\chi}_B < 0$, i.e., the initial field velocities are negative at the bounce.

proaches the slow-roll phase, and in the mixed-sign case the pathway to the phase can be prolonged dramatically.

Tables XIX and XX report the e-fold counts obtained when the initial field velocities have opposite signs ($\dot{\phi}_B > 0$, $\dot{\chi}_B < 0$), with the secondary field fixed at $\chi_B = 0.001 m_{\text{Pl}}$ while ϕ_B is varied (Table XIX), and with $\phi_B = 0.001 m_{\text{Pl}}$ while χ_B is varied (Table XX). Same results are displayed in Fig. 26.

The e-fold number N_{inf} is highly non-uniform and strongly sensitive to the chosen initial amplitudes. For varying ϕ_B (fixed $\chi_B = 0.001 m_{\text{Pl}}$), some initial values produce exceedingly large inflationary durations (for example $\phi_B = 1.6, 2.0, 3.0 m_{\text{Pl}}$ yield $N_{\text{inf}} \sim 10^3 - 10^4$), while neighboring values ($\phi_B = 1.8, 1.9 m_{\text{Pl}}$) produce effec-

tively zero e-folding in our integration window. This non-monotonic behaviour indicates that the system is passing close to different dynamical regimes even for small changes in the initial inflaton amplitude.

The runs with fixed small $\phi_B = 0.001 m_{\text{Pl}}$ and varying χ_B display a similarly irregular pattern. Several χ_B choices (e.g. $\chi_B = 37, 48, 52 m_{\text{Pl}}$) give huge N_{inf} , whereas other values ($\chi_B = 39, 40, 42 m_{\text{Pl}}$) produce moderate e-fold counts and still others ($\chi_B = 56, 57 m_{\text{Pl}}$) return zero within the integration interval.

The opposite sign velocity configuration naturally produces such sensitive dependence because the two fields initially move in opposite directions in field space. This can either plausibly slow the collective adiabatic motion

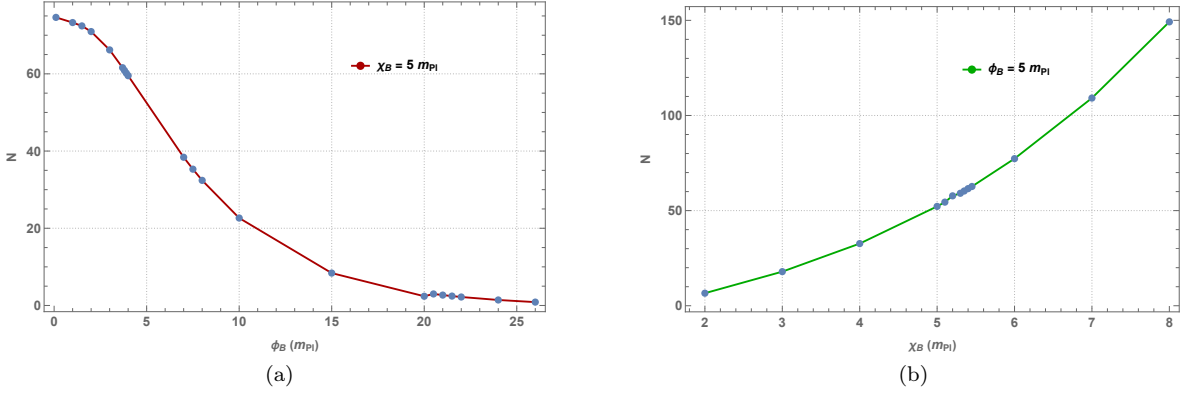


Figure 24. (a) Variation of the number of e-folds N_{inf} with respect to the initial value ϕ_B for a fixed $\chi_B = 5 m_{Pl}$. (b) Variation of the number of e-folds N_{inf} with respect to the initial value χ_B for fixed value of $\phi_B = 5 m_{Pl}$. The panels correspond to $\dot{\phi}_B < 0$ and $\dot{\chi}_B < 0$, i.e., both field velocities are negative at the bounce.

ϕ_B (m_{Pl})	t_{start} (m_{Pl}^{-1})	t_{end} (m_{Pl}^{-1})	$\ln(a_i)$	$\ln(a_f)$	N_{inf}
0.000001	178.0	130837	0.7888	15339.7655	15338.9767
0.00001	178.0	130826	0.7889	15339.6587	15338.8698
0.0001	178.0	130826	0.7889	15339.3968	15338.6078
0.001	178.0	130815	0.7892	15051.2187	15050.4295
0.01	178.0	130696	0.7927	15309.9294	15309.1366
0.1	177.9	129539	0.8008	15045.1123	15044.3114
1.0	176.3	118572	0.8141	12670.6684	12669.8542
2.0	173.9	107762	0.8547	10553.1916	10552.3368
3.0	170.8	98318	0.8921	8818.6867	8817.7945
4.0	167.1	89972	0.9275	7433.5488	7432.6212
5.0	162.8	82580	0.9402	6308.0909	6307.1507
6.0	158.3	76076	0.9802	5387.1998	5386.2196
8.0	148.5	65042	1.0202	3994.6655	3993.6452
10.0	138.8	56047	1.0810	3014.0289	3012.9479
15.0	117.11	39172	1.1875	1541.7755	1540.5880
20.0	100.1	25816	1.3122	718.2195	716.9073
25.0	81.7	4316	1.7724	40.4505	38.6780
26.0	88.0	259	2.0144	2.9895	0.9750
27.0	58.0	91	1.9021	2.2109	0.3088

Table XVII. This table shows the number of e-folds, N_{inf} , for various initial values of ϕ_B . The field value χ_B at the bounce is fixed at $1 m_{Pl}$. This case corresponds to $\dot{\phi}_B < 0$ and $\dot{\chi}_B > 0$, i.e., the initial field velocities have opposite signs at the bounce.

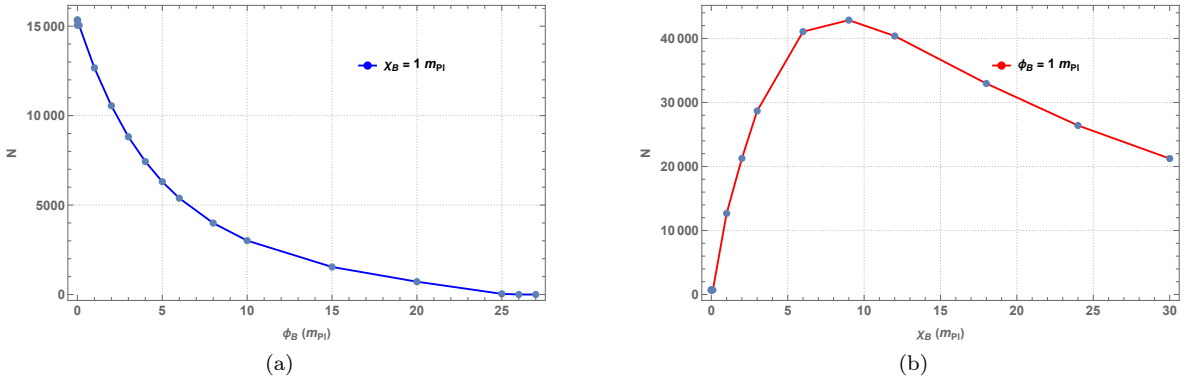


Figure 25. (a) Variation of the number of e-folds N with respect to the initial value ϕ_B for fixed value of $\chi_B = 1 m_{Pl}$. (b) Variation of the number of e-folds N_{inf} with respect to the initial value χ_B for fixed value of $\phi_B = 1 m_{Pl}$. The panels correspond to $\dot{\phi}_B < 0$ and $\dot{\chi}_B > 0$.

$\chi_B (m_{\text{Pl}})$	$t_{\text{start}} (m_{\text{Pl}}^{-1})$	$t_{\text{end}} (m_{\text{Pl}}^{-1})$	$\ln(a_i)$	$\ln(a_f)$	N_{inf}
0.000001	227.7	7406	0.9986	709.516	708.5173
0.00001	227.7	7371	0.9987	705.586	704.5872
0.0001	227.7	7371	0.9999	705.763	704.7630
0.001	227.7	7365	1.0119	705.728	704.7160
0.01	226.8	7317	1.0033	705.713	704.7096
0.1	219.0	6911	0.9827	705.841	704.8582
1.0	176.3	118558	0.8141	12670.5901	12669.7759
2.0	154.7	148968	0.7142	21267.5268	21266.8126
3.0	141.6	165469	0.6505	28682.0105	28681.3599
6.0	120.0	166852	0.5427	41062.4556	41061.9128
9.0	108.4	140971	0.4788	42864.1645	42863.6856
12.0	100.8	114247	0.4181	40382.1758	40381.7577
18.0	91.2	76070	0.3055	32958.9509	32958.6453
24.0	85.4	53598	0.1949	26404.0584	26403.8635
30.0	81.8	39685	0.1143	21243.7679	21243.6535

Table XVIII. This table shows the number of e-folds, N_{inf} , for various initial values of χ_B . Field value ϕ_B at bounce is fixed at $1 m_{\text{Pl}}$. This case corresponds to $\dot{\phi}_B < 0$ and $\dot{\chi}_B > 0$, i.e., the initial field velocities have opposite signs at the bounce.

$\phi_B (m_{\text{Pl}})$	$t_{\text{start}} (m_{\text{Pl}}^{-1})$	$t_{\text{end}} (m_{\text{Pl}}^{-1})$	$\ln(a_i)$	$\ln(a_f)$	N_{inf}
1.6	122.6	6523.6	0.6298	1214.7053	1214.0755
1.7	108.1	2154	1.0445	119.065	118.0205
1.8	157.4	182	0	0	0
1.9	256.46	257.29	2.37452×10^{-11}	2.37452×10^{-11}	0
2.0	216	177979	0.1748	45230.2595	45230.0847
3.0	204.1	95711	0.3094	36521.1788	36520.8694
4.0	178.2	11816	0.1600	6255.5883	6255.4283
5.0	180.7	12643	0.3635	5037.8257	5037.4622
6.0	200.2	19374	0.3183	7565.5620	7565.2437
6.1	199.5	18734	0.3383	7014.0839	7013.7456

Table XIX. Number of e-folds N_{inf} for various initial values of ϕ_B , corresponding to fixed $\chi_B = 0.001 m_{\text{Pl}}$. This case corresponds to $\dot{\phi}_B > 0$, $\dot{\chi}_B < 0$, i.e., the initial field velocities have opposite signs at the bounce.

$\chi_B (m_{\text{Pl}})$	$t_{\text{start}} (m_{\text{Pl}}^{-1})$	$t_{\text{end}} (m_{\text{Pl}}^{-1})$	$\ln(a_i)$	$\ln(a_f)$	N_{inf}
37	107.4	3311	0.2899	1364.3173	1364.0274
38	97.1	1890	0.5929	366.3120	365.7190
39	93	984	0.9258	47.0069	46.0810
40	95	453	1.2947	11.8853	10.5905
42	103.5	441	1.5582	6.0032	4.4449
44	96.6	5955	1.3690	116.177	114.808
48	98	1026	0.5162	1684.7690	1684.2527
52	113	7480	0.1135	4231.055	4230.9419
56	35.6	39.9	2.28175×10^{-11}	2.28175×10^{-11}	0
57	35.59	39.97	2.28166×10^{-11}	2.28166×10^{-11}	0

Table XX. Number of e-folds N_{inf} for various initial values of χ_B for the case corresponds to $\dot{\phi}_B > 0$, $\dot{\chi}_B < 0$.

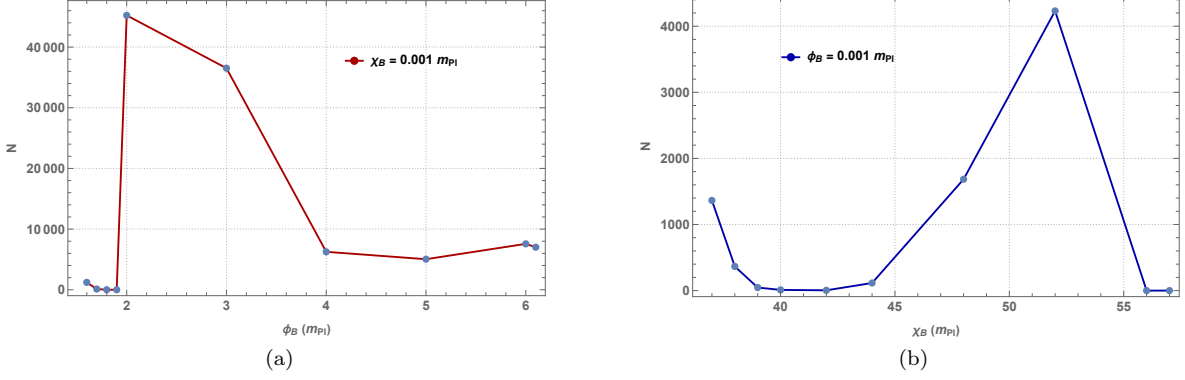


Figure 26. (a) Variation of the number of e-folds N_{inf} with respect to ϕ_B for fixed $\chi_B = 0.001 m_{Pl}$. (b) Variation of the number of e-folds N_{inf} with respect to χ_B for fixed $\phi_B = 0.001 m_{Pl}$. The panels correspond to the case $\dot{\phi}_B > 0$, $\dot{\chi}_B < 0$.

and keep the system near a potential-dominated region for extended periods or induce rapid excursion away from the inflationary valley depending on the exact amplitude. Hence, the mixed sign outcomes produce the observed large scatter.

The pre-inflationary number of e-folds for this model is found to lie in the range $N_{\text{preinf}} \approx 1-3$ across the scanned phase space for all velocity sign configurations. Although this value is larger than that obtained for the first model, it remains relatively small and therefore does not contribute significantly to the overall expansion of the universe.

The treatment of analytical background solutions for this model is included in the Appendix A.

B. Qualitative Analysis: Dynamical System Approach

Following the methods in [33, 46, 72, 84, 85], we define the following dimensionless variables to construct an autonomous dynamical system by using the energy density equation:

$$\begin{aligned} x_\phi &\equiv \frac{\dot{\phi}}{\sqrt{2\rho_c}}, & x_\chi &\equiv \frac{\dot{\chi}}{\sqrt{2\rho_c}}, & x_\Phi &\equiv \frac{\dot{\Phi}}{\sqrt{2\rho_c}}, \\ y_\phi &\equiv \beta\phi, & y_\chi &\equiv \frac{g\chi}{m}, & y_\Phi &\equiv \frac{\Phi}{m} \end{aligned} \quad (5.1)$$

Similar to the previous model, we define $z \equiv \frac{\rho}{\rho_c}$. Substituting this definition into the modified Friedmann equation (2.15a) again produces the constraint eq. (4.5). The constraint obtained by substituting the definitions (5.1) in the energy density equation:

$$z = x_\phi^2 + e^{2y_\phi} x_\chi^2 + x_\Phi^2 + \frac{m^2}{2\beta^2\rho_c} y_\phi^2 (1 + y_\chi^2). \quad (5.2)$$

As discussed in the hybrid model (4.7) analysis, the modified Friedmann equation in LQC restricts the energy density to the bounded interval $0 \leq z \leq 1$. Consequently, the physical phase space of the dynamical system is not the

full unconstrained space of the variables, but a compact submanifold defined by the energy–density constraint.

To make this bounded structure explicit, we adopt the same trigonometric compactification [87] introduced previously in Eq. (4.7), which automatically enforces the LQC bound on the energy density. In terms of this variable, the modified Friedmann equation again splits into two branches corresponding to the expanding ($H > 0$) and contracting ($H < 0$) phases, with the bounce occurring at $\theta = \frac{\pi}{2}$.

Applying this compactification to the two-field interaction model, the energy–density constraint (5.2) becomes

$$\sin^2 \theta = x_\phi^2 + e^{2y_\phi} x_\chi^2 + x_\Phi^2 + \frac{m^2}{2\beta^2\rho_c} y_\phi^2 (1 + y_\chi^2). \quad (5.3)$$

Thus, the autonomous system evolves on a compact phase–space manifold, and the admissible fixed points must satisfy both the compactified constraints above. As in the hybrid model, the trigonometric parametrization provides a global description of the contracting and expanding branches within a single bounded phase space.

We define the dimensionless evolution parameter $\tau \equiv \frac{t}{\beta}$ so that the time derivative transforms as $\frac{d}{dt} = \beta \frac{d}{d\tau}$.

Using this relation and the definitions in Eq. (5.1), the closed autonomous system governing the evolution of the dimensionless variables takes the form

$$\frac{dx_\phi}{d\tau} = -3\beta H x_\phi + \sqrt{2\rho_c} \beta^2 e^{2y_\phi} x_\chi^2 - \frac{m^2}{\sqrt{2\rho_c}} y_\phi - \frac{m^2}{\sqrt{2\rho_c}} y_\phi y_\chi^2, \quad (5.4)$$

$$\frac{dx_\chi}{d\tau} = -3\beta H x_\chi - 2\beta x_\phi x_\chi - \frac{gm}{\beta\sqrt{2\rho_c}} e^{-2y_\phi} y_\phi^2 y_\chi, \quad (5.5)$$

$$\frac{dx_\Phi}{d\tau} = -3\beta H x_\Phi, \quad (5.6)$$

$$\frac{dy_\phi}{d\tau} = \beta^2 \sqrt{2\rho_c} x_\phi, \quad (5.7)$$

$$\frac{dy_\chi}{d\tau} = \frac{\beta g}{m} \sqrt{2\rho_c} x_\chi, \quad (5.8)$$

$$\frac{dy_\Phi}{d\tau} = \frac{\beta}{m} \sqrt{2\rho_c} x_\Phi. \quad (5.9)$$

To investigate the asymptotic behavior of the dynamical system, we analyze its fixed points by finding those phase space points where all autonomous variables become stationary. To investigate the local stability properties of the fixed points, we linearize the autonomous system around each fixed point by computing the Jacobian matrix. The Jacobian encodes how small perturbations evolve in the vicinity of a fixed point, and its eigenvalues determine the nature of stability.

All fixed points obtained in the system correspond to configurations in which the kinetic contributions of all scalar fields vanish, while the potential energy of the χ sector remains arbitrary but non-zero. Consequently, the total energy density is entirely potential dominated, leading to an effective equation of state $\omega = -1$.

These solutions therefore represent de Sitter-type cosmological regimes. The scale factor evolves exponentially in the expanding branch and contracts exponentially in the contracting branch.

The presence of arbitrary values in (y_χ, y_Φ) phase-space coordinates indicates that the equilibrium configurations form a continuous manifold rather than isolated points. This reflects the existence of flat directions in the potential, along which the gradient of the potential vanishes identically. Consequently, the fixed points correspond to degenerate stationary configurations and their stability cannot be determined from linear analysis alone.

The purely imaginary eigenvalues signal oscillatory perturbations around this locus. Thus, the inflationary solution is a center manifold of de Sitter states.

VI. CONCLUSION

This paper begins by extending LQC framework to a generic multi-field setting characterized by a non-trivial field-space metric G_{IJ} , that allows for kinetic couplings among the component fields. The cosmological system is canonically formulated in the backdrop of LQG, where GR admits a Yang–Mills-type phase-space structure in terms of the Ashtekar variables, refer II A. Implementing the holonomy representation enables the quantization of the gravitational sector coupled to the multi-field system. The resulting effective description, obtained using the improved $\bar{\mu}$ -scheme polymerization, refer II B, yields quantum-corrected equations of motion governing the background dynamics, refer II C. We then numerically evolve the two representative models starting from KED quantum bounce to obtain the pre-inflationary and inflationary regimes in the direction of expanding universe, for different initial fields and their velocity signs configurations, refer Subsections IV A and V A.

As expected, the robustness of the quantum bounce is confirmed, with the regularization of the classical big-bang singularity. Independent of the potential model or initial field amplitudes, the system consistently enters a superinflationary phase driven purely by loop quantum corrections and ends when $\rho = \rho_c/2$, at which point the effect of quantum corrections weakens and the universe undergoes a transition phase in which Hubble friction rapidly suppresses the kinetic energy of the scalar fields, enabling transition to a potential-dominated slow-roll phase, refer tables I and XII.

A key outcome of this study is the strong sensitivity of inflationary dynamics to the pre-inflationary initial conditions, including the relative signs of the field velocities at the bounce, refer tables II–X and Figs. 11–14 for hybrid model and tables XIII–XX and Figs. 23–26 for string-inspired model. These results highlight the intricate interplay between quantum geometric corrections and multi-field interactions, and indicate that achieving the observationally required $N_{\text{inf}} \gtrsim 60$ e-folds in the models considered often necessitates specific parameter choices or finely tuned initial conditions. For both models considered, the contribution of the pre-inflationary dynamics to the total expansion remains small, typically not exceeding 4 e-folds.

In addition, in our analysis we have found that the choice of different values of the clock field at bounce does not affect the physical results derived for the models. This is because the kinetic energy of the clock field quickly dilutes to zero owing to its massless nature. This is also signified by the saturation value as tabulated in IV B, V B. In order to present a typical example, the change in N_{inf} is 0.09 from $\dot{\Phi}_B = 0.1 m_{Pl}^2$ to $\dot{\Phi}_B = 0.8 m_{Pl}^2$ for $\Phi_B = 2 m_{Pl}$ and parameter values $g = 10^{-5}, \lambda = 0.3, m = 0.01 m_{Pl}, M = 1 m_{Pl}$ for the hybrid model.

A comparison between the hybrid and string-inspired models reveals qualitatively different phase-space structures despite their common LQC origin, refer IV B and V B. In both systems, the modified Friedmann equation restricts the physical phase space to a compact region, and the presence of the clock field introduces a neutral direction, leading to loci of fixed points rather than isolated equilibria.

In the hybrid model, refer table IV B three distinct sets of critical points arise at $y_\chi = -1, 0, +1$. The points at $y_\chi = \pm 1$ form one-dimensional lines of equilibria parameterized by the clock-field variable y_Φ , and they behave as non-hyperbolic centers with purely imaginary eigenvalues. By contrast, the point at $y_\chi = 0$ behaves as a saddle, with stability properties that reverse between the expanding and contracting branches. This indicates that the $\chi = 0$ configuration acts as a transient or repulsive state, while the symmetry-broken vacua at $y_\chi = \pm 1$ correspond to neutral configurations.

The string-inspired model, refer table V B exhibits a higher degree of degeneracy. Instead of isolated lines, it admits a two-dimensional surface of fixed points pa-

Point	Fixed point coordinates	Eigenvalues	Linear stability
Expanding branch ($H > 0$)			
$Q_1^{(+)}$	$(x_\phi, x_\chi, x_\Phi, y_\phi, y_\chi, y_\Phi)$ $= (0, 0, 0, 0, \bar{y}_\chi, \bar{y}_\Phi)$	$\{0, 0, 0, 0, \pm 3 \times 10^{-6} i \sqrt{1 + \bar{y}_\chi^2}\}$	Non-hyperbolic center
Contracting branch ($H < 0$)			
$Q_1^{(-)}$	$(x_\phi, x_\chi, x_\Phi, y_\phi, y_\chi, y_\Phi)$ $= (0, 0, 0, 0, \bar{y}_\chi, \bar{y}_\Phi)$	$\{0, 0, 0, 0, \pm 3 \times 10^{-6} i \sqrt{1 + \bar{y}_\chi^2}\}$	Non-hyperbolic center

Table XXI. Critical points of the string-inspired model in LQC dynamical system. The modified Friedmann equation admits two branches corresponding to $H > 0$ (expanding phase) and $H < 0$ (contracting phase). An overbar denotes an arbitrary constant value along that direction, indicating a continuous locus of equilibrium points rather than an isolated critical point. In this model, both branches yield the same fixed-point structure and eigenvalue spectrum.

parameterized by both y_χ and y_Φ . All eigenvalues either vanish or are purely imaginary, implying that the system is entirely non-hyperbolic near these equilibria. Furthermore, the expanding and contracting branches share identical eigenvalue spectra, indicating a symmetric dynamical structure around the bounce.

This contrast reflects the different scalar field interactions and field-space geometry of the two models, leading to qualitatively distinct cosmological phase-space evolutions, even though both are governed by the same compactified LQC dynamics that ensures bounded trajectories and the avoidance of classical singularities.

Future work aims to extend the present analysis by incorporating perturbative dynamics, refer [89] for single field case, enabling the computation of power spectra and spectral indices to confront the model predictions with CMB observations. From a theoretical perspective, exploring a broader class of potentials, multi-field forms such as product-exponential, axion-like, power-law will help assess the universality and robustness of the inflationary features identified here. In parallel, extending the dynamical systems framework to include higher-order stability analysis can reveal non-linear stability structures. Finally, comparing the evolution across different geometries of the field space, while keeping the rest of the setup identical, can shed light on how field-space curvature and non-trivial metric couplings influence the quantum-corrected cosmological evolution. Together, these extensions will provide a comprehensive understanding of multi-field inflation in LQC.

ACKNOWLEDGMENTS

M.S. acknowledges Mahidol University (Fundamental Fund: fiscal year 2025 by National Science Research and Innovation Fund (NSRF)); R.O.R. acknowledges financial support through research grants from Conselho Nacional de Desenvolvimento Científico e Tecnológico (CNPq), Grant No. 307286/2021-5, and from Fundação Carlos Chagas Filho de Amparo à Pesquisa do Estado do Rio de Janeiro (FAPERJ), Grant No. E-26/200.415/2026.

Appendix A: Analytical solutions to the background dynamics

In this section, we present analytical solutions for the background dynamics in LQC following the methods in [67]. The analysis is performed in successive phases corresponding to dominant physical effects, starting from the bounce and leading up to the slow-roll inflationary phase.

During the bounce and superinflation phase, the dynamics are dominated by the kinetic energy of the scalar field, so that $\rho \simeq \frac{1}{2}\dot{\sigma}^2$ and $V \ll K$. The Klein-Gordon equation for the average field σ reduces to

$$\ddot{\sigma} + 3H\dot{\sigma} \simeq 0. \quad (\text{A1})$$

Defining $u(t) \equiv \dot{\sigma}(t)$, we have

$$\dot{u} + 3Hu = 0 \quad \Rightarrow \quad \dot{\sigma}(t) = \dot{\sigma}_B \left(\frac{a_B}{a(t)} \right)^3, \quad (\text{A2})$$

where $\dot{\sigma}_B = \sqrt{2\rho_c}$ from the bounce condition $\rho_B = \rho_c$

Substituting into the effective LQC Friedmann equation

$$H^2 = \frac{\kappa}{3}\rho \left(1 - \frac{\rho}{\rho_c} \right), \quad \rho(t) = \rho_c \left(\frac{a_B}{a(t)} \right)^6, \quad (\text{A3})$$

and defining the characteristic bounce timescale

$$t_B^2 \equiv \frac{1}{3\kappa\rho_c}, \quad (\text{A4})$$

the analytical solutions for the scale factor and the field are

$$\begin{aligned} a(t) &= a_B \left(1 + \frac{t^2}{t_B^2} \right)^{1/6}, & \dot{a}(t) &= \frac{a_B t}{3t_B^2} \left(1 + \frac{t^2}{t_B^2} \right)^{-5/6}, \\ H(t) &= \frac{t}{3(t_B^2 + t^2)}, & \dot{H}(t) &= \frac{t_B^2 - t^2}{3(t_B^2 + t^2)^2}, \\ \rho(t) &= \rho_c \left(1 + \frac{t^2}{t_B^2} \right)^{-1}, & \dot{\sigma}(t) &= \sqrt{2\rho_c} \left(1 + \frac{t^2}{t_B^2} \right)^{-1/2}, \\ \sigma(t) &= \sigma_B + \sqrt{2\rho_c} t_B \operatorname{arsinh} \left(\frac{t}{t_B} \right). \end{aligned}$$

The above solutions are valid throughout the bounce and superinflation phase, where the kinetic-dominated approximation holds.

Let t_c denote the transition time where kinetic and potential energies are equal,

$$\frac{1}{2}\dot{\sigma}_c^2 = V(\sigma_c) \quad \Rightarrow \quad \dot{\sigma}_c^2 = 2V(\sigma_c), \quad (\text{A5})$$

and let t_i denote the onset of slow-roll ($\omega = -1/3$), for which

$$\dot{\sigma}_i^2 = V(\sigma_i). \quad (\text{A6})$$

Expanding the background in logarithmic time $x \equiv \ln(t/t_c)$ and keeping first-order terms, we write

$$\sigma(t) \simeq \sigma_c + t_c \dot{\sigma}_c \ln \frac{t}{t_c}, \quad (\text{A7})$$

$$\dot{\sigma}(t) \simeq \dot{\sigma}_c \frac{t_c}{t}, \quad (\text{A8})$$

$$a(t) \simeq a_c \left(1 + t_c H_c \ln \frac{t}{t_c} \right) \quad (\text{A9})$$

Evaluating at $t = t_i$, we obtain

$$\sigma_i = \sigma_c + t_c \dot{\sigma}_c \ln \frac{t_i}{t_c}, \quad (\text{A10})$$

$$\dot{\sigma}_i = \dot{\sigma}_c \frac{t_c}{t_i}, \quad (\text{A11})$$

$$a_i = a_c \left(1 + t_c H_c \ln \frac{t_i}{t_c} \right), \quad (\text{A12})$$

and the onset condition gives

$$\frac{t_i}{t_c} = \sqrt{\frac{2V(\sigma_c)}{V(\sigma_i)}}, \quad \exp\left(-\frac{2(\sigma_i - \sigma_c)}{t_c \dot{\sigma}_c}\right) = \frac{V(\sigma_i)}{2V(\sigma_c)}. \quad (\text{A13})$$

For a first-order expansion of the potential near t_c ,

$$V(\sigma_i) \simeq V_c + V_c' t_c \dot{\sigma}_c \ln \frac{t_i}{t_c}, \quad \dot{\sigma}_c = \pm \frac{t_i}{t_c} \sqrt{V_c + V_c' t_c \dot{\sigma}_c \ln(t_i/t_c)}. \quad (\text{A14})$$

Thus, for the models under consideration, the potential solutions reduce to,

$$V(\phi_i, \chi_i) \simeq V(\phi_c, \chi_c) + \partial_\phi V|_c (\phi_i - \phi_c) + \partial_\chi V|_c (\chi_i - \chi_c) \quad (\text{A15})$$

a. Hybrid inflation model:

$$\dot{\sigma}_c^2 = m^2 \phi_c^2 + g^2 \phi_c^2 \chi_c^2 + \frac{\lambda}{2} (\chi_c^2 - M^2)^2. \quad (\text{A16})$$

b. String-inspired model:

$$\dot{\sigma}_c^2 = m^2 \phi_c^2 + g^2 \phi_c^2 \chi_c^2. \quad (\text{A17})$$

For $t > t_i$, the potential dominates and the slow-roll conditions

$$\frac{1}{2}\dot{\sigma}^2 \ll V(\phi, \chi), \quad |\ddot{\sigma}| \ll 3H|\dot{\sigma}|, \quad (\text{A18})$$

reduce the equations to

$$H^2 \simeq \frac{8\pi}{3m_{\text{Pl}}^2} V(\phi, \chi), \quad (\text{A19})$$

$$3H\dot{\sigma} + \frac{\partial V}{\partial \sigma} \simeq 0, \quad \frac{\partial V}{\partial \sigma} = \frac{\dot{\phi}}{\dot{\sigma}} \frac{\partial V}{\partial \phi} + \frac{\dot{\chi}}{\dot{\sigma}} \frac{\partial V}{\partial \chi}. \quad (\text{A20})$$

Integrating yields

$$\int_{\sigma_i}^{\sigma(t)} d\sigma \frac{V(\sigma)}{\partial V/\partial \sigma} \simeq -\frac{m_{\text{Pl}}^2}{8\pi} (t - t_i), \quad (\text{A21})$$

$$a(t) \simeq a_i e^{H_{\text{inf}}(t-t_i)}, \quad (\text{A22})$$

$$H_{\text{inf}}^2 \simeq \frac{8\pi}{3m_{\text{Pl}}^2} V(\sigma_i). \quad (\text{A23})$$

-
- [1] Abhay Ashtekar and Parampreet Singh. Loop Quantum Cosmology: A Status Report. *Class. Quant. Grav.*, 28:213001, 2011.
- [2] Ivan Agulló, Anzhong Wang, and Edward Wilson-Ewing. Loop quantum cosmology: relation between theory and observations. *Handbook of Quantum Gravity*, 1 2023.
- [3] Bao-Fei Li and Parampreet Singh. *Loop Quantum Cosmology: Physics of Singularity Resolution and Its Implications*. Springer, 2024.
- [4] Abhay Ashtekar, Martin Bojowald, and Jerzy Lewandowski. Mathematical structure of loop quantum cosmology. *Adv. Theor. Math. Phys.*, 7(2):233–268, 2003.
- [5] Martin Bojowald. Loop quantum cosmology. *Living Rev. Rel.*, 8:11, 2005.
- [6] Abhay Ashtekar. Loop quantum cosmology: an overview. *General Relativity and Gravitation*, 41(4):707–741, February 2009.
- [7] Kinjal Banerjee, Gianluca Calcagni, and Mercedes Martin-Benito. Introduction to loop quantum cosmology. *SIGMA*, 8:016, 2012.
- [8] Abhay Ashtekar. Symmetry reduced loop quantum gravity: A bird’s eye view. *Int. J. Mod. Phys. D*, 25(08):1642010, 2016.
- [9] Martin Bojowald. Loop quantum cosmology. I. Kinematics. *Class. Quant. Grav.*, 17:1489–1508, 2000.
- [10] Abhay Ashtekar, Tomasz Pawłowski, and Parampreet Singh. Quantum Nature of the Big Bang: Improved dynamics. *Phys. Rev. D*, 74:084003, 2006.
- [11] Abhay Ashtekar, Alejandro Corichi, and Parampreet Singh. Robustness of key features of loop quantum cosmology. *Phys. Rev. D*, 77:024046, 2008.
- [12] Martin Bojowald. Absence of singularity in loop quantum cosmology. *Phys. Rev. Lett.*, 86:5227–5230, 2001.
- [13] Parampreet Singh. Are loop quantum cosmos never singular? *Class. Quant. Grav.*, 26:125005, 2009.
- [14] Parampreet Singh. Loop quantum cosmology and the fate of cosmological singularities. *Bull. Astron. Soc. India*, 42:121, 2014.
- [15] Abhay Ashtekar and Edward Wilson-Ewing. Loop quantum cosmology of Bianchi I models. *Phys. Rev. D*, 79:083535, 2009.
- [16] Manabendra Sharma, Tao Zhu, and Anzhong Wang. Background dynamics of pre-inflationary scenario in Brans-Dicke loop quantum cosmology. *Commun. Theor. Phys.*, 71(10):1205–1218, 2019.
- [17] Manabendra Sharma, Gustavo S. Vicente, Leila L. Graef, Rudnei O. Ramos, and Anzhong Wang. Quantum geometric formulation of Brans-Dicke theory for Bianchi I spacetime. *Phys. Rev. D*, 111(4):043501, 2025.
- [18] Dah-Wei Chiou. Effective dynamics, big bounces and scaling symmetry in Bianchi type I loop quantum cosmology. *Phys. Rev. D*, 76:124037, 2007.
- [19] M. Martin-Benito, G. A. Mena Marugan, and T. Pawłowski. Loop Quantization of Vacuum Bianchi I Cosmology. *Phys. Rev. D*, 78:064008, 2008.
- [20] Abhay Ashtekar and Edward Wilson-Ewing. Loop quantum cosmology of Bianchi type II models. *Phys. Rev. D*, 80:123532, 2009.
- [21] Edward Wilson-Ewing. Loop quantum cosmology of Bianchi type IX models. *Phys. Rev. D*, 82:043508, 2010.
- [22] Brajesh Gupt and Parampreet Singh. Quantum gravitational Kasner transitions in Bianchi-I spacetime. *Phys. Rev. D*, 86:024034, 2012.
- [23] Parampreet Singh and Edward Wilson-Ewing. Quantization ambiguities and bounds on geometric scalars in anisotropic loop quantum cosmology. *Class. Quant. Grav.*, 31:035010, 2014.
- [24] Parampreet Singh. Is classical flat Kasner spacetime flat in quantum gravity? *Int. J. Mod. Phys. D*, 25(08):1642001, 2016.
- [25] David Brizuela, Guillermo A. D Mena Marugan, and Tomasz Pawłowski. Big Bounce and inhomogeneities. *Class. Quant. Grav.*, 27:052001, 2010.
- [26] Wen-Cong Gan, Leila L. Graef, Rudnei O. Ramos, Gustavo S. Vicente, and Anzhong Wang. Quantum damping of cosmological shear: A new prediction from loop quantum cosmologies. *arXiv preprint*, 10 2025.
- [27] Abhay Ashtekar and David Sloan. Probability of Inflation in Loop Quantum Cosmology. *Gen. Rel. Grav.*, 43:3619–3655, 2011.
- [28] Bao-Fei Li, Parampreet Singh, and Anzhong Wang. Genericness of pre-inflationary dynamics and probability of the desired slow-roll inflation in modified loop quantum cosmologies. *Phys. Rev. D*, 100(6):063513, 2019.
- [29] Linda Linsefors and Aurelien Barrau. Duration of inflation and conditions at the bounce as a prediction of effective isotropic loop quantum cosmology. *Phys. Rev. D*, 87(12):123509, 2013.
- [30] L. N. Barboza, L. L. Graef, and Rudnei O. Ramos. Warm bounce in loop quantum cosmology and the prediction for the duration of inflation. *Phys. Rev. D*, 102(10):103521, 2020.
- [31] L. N. Barboza, G. L. L. W. Levy, L. L. Graef, and Rudnei O. Ramos. Constraining the Barbero-Immirzi parameter from the duration of inflation in loop quantum cosmology. *Phys. Rev. D*, 106(10):103535, 2022.
- [32] Alejandro Corichi and Asieh Karami. Measure problem in slow roll inflation and loop quantum cosmology. *Phys. Rev. D*, 83:104006, May 2011.
- [33] Manabendra Sharma, M. Shahalam, Qiang Wu, and Anzhong Wang. Preinflationary dynamics in loop quantum cosmology: monodromy potential. *Journal of Cosmology and Astroparticle Physics*, 2018(11):003–003, November 2018.
- [34] Jakub Mielczarek. Possible observational effects of loop quantum cosmology. *Phys. Rev. D*, 81:063503, 2010.
- [35] L. L. Graef and Rudnei O. Ramos. Probability of Warm Inflation in Loop Quantum Cosmology. *Phys. Rev. D*, 98(2):023531, 2018.
- [36] Micol Benetti, Leila Graef, and Rudnei O. Ramos. Observational constraints on warm inflation in loop quantum cosmology. *JCAP*, 2019(10):066, 2019.
- [37] G. L. L. W. Levy and Rudnei O. Ramos. α -attractor potentials in loop quantum cosmology. *Phys. Rev. D*, 110(4):043507, 2024.
- [38] Evan Ranken and Parampreet Singh. Nonsingular power-law and assisted inflation in loop quantum cosmology. *Phys. Rev. D*, 85:104002, May 2012.
- [39] Andronikos Paliathanasis and Genly Leon. Hyperbolic inflationary model with nonzero curvature. *Phys. Lett. B*, 834:137407, 2022.

- [40] Chong-Bin Chen and Jiro Soda. Geometric structure of multi-form-field isotropic inflation and primordial fluctuations. *JCAP*, 05(05):029, 2022.
- [41] Mariaveronica De Angelis and Carsten van de Bruck. Adiabatic and isocurvature perturbations in extended theories with kinetic couplings. *JCAP*, 10:023, 2023.
- [42] Shuntaro Mizuno and Shinji Mukohyama. Primordial perturbations from inflation with a hyperbolic field-space. *Phys. Rev. D*, 96:103533, Nov 2017.
- [43] Adam R. Brown. Hyperbolic Inflation. *Phys. Rev. Lett.*, 121(25):251601, 2018.
- [44] David H. Lyth and Antonio Riotto. Particle physics models of inflation and the cosmological density perturbation. *Phys. Rept.*, 314:1–146, 1999.
- [45] Andrei D. Linde. Hybrid inflation. *Phys. Rev. D*, 49:748–754, 1994.
- [46] Rudnei O. Ramos. Fine tuning solution for hybrid inflation in dissipative chaotic dynamics. *Phys. Rev. D*, 64:123510, 2001.
- [47] Andrei D. Linde and Antonio Riotto. Hybrid inflation in supergravity. *Phys. Rev. D*, 56:R1841–R1844, 1997.
- [48] Thomas Cailleteau, Linda Linsefors, and Aurelien Barrau. Anomaly-free perturbations with inverse-volume and homology corrections in Loop Quantum Cosmology. *Class. Quant. Grav.*, 31:125011, 2014.
- [49] J. Grain, A. Barrau, and A. Gorecki. Inverse volume corrections from loop quantum gravity and the primordial tensor power spectrum in slow-roll inflation. *Phys. Rev. D*, 79:084015, 2009.
- [50] Dah-Wei Chiou and Kai Liu. Cosmological inflation driven by homology corrections of loop quantum cosmology. *Phys. Rev. D*, 81:063526, 2010.
- [51] Edward Wilson-Ewing. Homology Corrections in the Effective Equations for Scalar Mode Perturbations in Loop Quantum Cosmology. *Class. Quant. Grav.*, 29:085005, 2012.
- [52] Alejandro Corichi and Asieh Karami. Loop quantum cosmology of $k = 1$ FLRW: Effects of inverse volume corrections. *Class. Quant. Grav.*, 31:035008, 2014.
- [53] Laura Iacconi and David J. Mulryne. Multi-field inflation with large scalar fluctuations: non-Gaussianity and perturbativity. *JCAP*, 09:033, 2023.
- [54] Debottam Nandi and S. Shankaranarayanan. Complete Hamiltonian analysis of cosmological perturbations at all orders II: Non-canonical scalar field. *JCAP*, 10:008, 2016.
- [55] Xiangdong Zhang. Loop Quantum Cosmology, Modified Gravity and Extra Dimensions. *Universe*, 2(3):15, 2016.
- [56] Alejandro Corichi and Parampreet Singh. Is loop quantization in cosmology unique? *Phys. Rev. D*, 78:024034, 2008.
- [57] Krzysztof A. Meissner. Black hole entropy in loop quantum gravity. *Class. Quant. Grav.*, 21:5245–5252, 2004.
- [58] Rakshit P. Vyas and Mihir J. Joshi. The Barbero–Immirzi Parameter: An Enigmatic Parameter of Loop Quantum Gravity. *Physics*, 4:1094–1116, 2022.
- [59] Abhay Ashtekar, Tomasz Pawłowski, and Parampreet Singh. Quantum nature of the big bang: An analytical and numerical investigation. *Phys. Rev. D*, 73:124038, Jun 2006.
- [60] Gabriele Barca, Eleonora Giovannetti, and Giovanni Montani. An Overview on the Nature of the Bounce in LQC and PQM. *Universe*, 7(9):327, 2021.
- [61] Wen-Cong Gan, Xiao-Mei Kuang, Zhen-Hao Yang, Yungui Gong, Anzhong Wang, and Bin Wang. Nonexistence of quantum black and white hole horizons in an improved dynamic approach. *Sci. China Phys. Mech. Astron.*, 67(8):280411, 2024.
- [62] Abhay Ashtekar, Tomasz Pawłowski, and Parampreet Singh. Quantum nature of the big bang. *Phys. Rev. Lett.*, 96:141301, Apr 2006.
- [63] Abhay Ashtekar and David Sloan. Loop quantum cosmology and slow roll inflation. *Physics Letters B*, 694(2):108–112, 2010.
- [64] Parampreet Singh, Kevin Vandersloot, and G. V. Vereshchagin. Non-singular bouncing universes in loop quantum cosmology. *Phys. Rev. D*, 74:043510, 2006.
- [65] Xin Zhang and Yi Ling. Inflationary universe in loop quantum cosmology. *JCAP*, 08:012, 2007.
- [66] Tao Zhu, Anzhong Wang, Klaus Kirsten, Gerald Cleaver, and Qin Sheng. Universal features of quantum bounce in loop quantum cosmology. *Phys. Lett. B*, 773:196–202, 2017.
- [67] Tao Zhu, Anzhong Wang, Gerald Cleaver, Klaus Kirsten, and Qin Sheng. Pre-inflationary universe in loop quantum cosmology. *Phys. Rev. D*, 96(8):083520, 2017.
- [68] Jamal Saeed, Rui Pan, Christian Brown, Gerald Cleaver, Gerald Cleaver, and Anzhong Wang. Universal Properties of the Evolution of the Universe in Modified Loop Quantum Cosmology. *Universe*, 10(10):397, 2024.
- [69] Bao-Fei Li, Parampreet Singh, and Anzhong Wang. Phenomenological implications of modified loop cosmologies: an overview. *Front. Astron. Space Sci.*, 8:701417, 2021.
- [70] Bao-Fei Li, Parampreet Singh, and Anzhong Wang. Qualitative dynamics and inflationary attractors in loop cosmology. *Phys. Rev. D*, 98(6):066016, 2018.
- [71] Anshuman Bhardwaj, Edmund J. Copeland, and Jorma Louko. Inflation in loop quantum cosmology. *Phys. Rev. D*, 99:063520, Mar 2019.
- [72] M. Shahalam, Manabendra Sharma, Qiang Wu, and Anzhong Wang. Preinflationary dynamics in loop quantum cosmology: Power-law potentials. *Phys. Rev. D*, 96:123533, Dec 2017.
- [73] Kui Xiao, Xiao-Kai He, and Jian-Yang Zhu. Note on the super-inflation in loop quantum cosmology. *Physics Letters B*, 727(4):349–356, 2013.
- [74] Daniel Baumann. Tasi lectures on inflation, 2012.
- [75] Arjun Berera, Heliudson Bernardo, Suddhasattwa Brahma, Jaime Calderón-Figueroa, Rudnei O. Ramos, and Michael W. Toomey. Heterotic Warm Inflation. 9 2025.
- [76] Carsten van de Bruck and Mathew Robinson. Power Spectra beyond the Slow Roll Approximation in Theories with Non-Canonical Kinetic Terms. *JCAP*, 08:024, 2014.
- [77] C. Sivaram. What is special about the Planck mass? 7 2007.
- [78] Marco Baldi, Fabio Finelli, and Sabino Matarrese. Inflation with violation of the null energy condition. *Phys. Rev. D*, 72:083504, 2005.
- [79] Sebastien Clesse. Hybrid inflation along waterfall trajectories. *Phys. Rev. D*, 83:063518, 2011.
- [80] David H. Lyth. The hybrid inflation waterfall and the primordial curvature perturbation. *JCAP*, 05:022, 2012.
- [81] Hideo Kodama, Kazunori Kohri, and Kazunori Nakayama. On the waterfall behavior in hybrid inflation. *Prog. Theor. Phys.*, 126:331–350, 2011.
- [82] Edmund J. Copeland, Andrew R. Liddle, David H. Lyth, Ewan D. Stewart, and David Wands. False vacuum inflation with einstein gravity. *Phys. Rev. D*, 49:6410–6433,

- Jun 1994.
- [83] Michele Cicoli, Giuseppe Dibitetto, and Francisco G. Pedro. Out of the Swampland with Multifield Quintessence? *JHEP*, 10:035, 2020.
- [84] Daris Samart and Burin Gumjudpai. Phantom field dynamics in loop quantum cosmology. *Phys. Rev. D*, 76:043514, 2007.
- [85] Suratna Das, Saddam Hussain, Debottam Nandi, Rudnei O. Ramos, and Renato Silva. Stability analysis of warm quintessential dark energy model. *Phys. Rev. D*, 108(8):083517, 2023.
- [86] N. Dimakis, A. Paliathanasis, Petros A. Terzis, and T. Christodoulakis. Cosmological Solutions in Multiscale Field Theory. *Eur. Phys. J. C*, 79(7):618, 2019.
- [87] Christian G. Böhrer and Nyein Chan. *Dynamical Systems in Cosmology*, chapter Chapter 4, pages 121–156. World Scientific, 2017.
- [88] Steven H. Strogatz. *Nonlinear Dynamics and Chaos*. CRC Press, 2nd edition, 2018.
- [89] Martin Bojowald, Golam Mortuza Hossain, Mikhail Kagan, and S. Shankaranarayanan. Anomaly freedom in perturbative loop quantum gravity. *Phys. Rev. D*, 78:063547, 2008.